This is a preprint, the final version is subject to change, of the American Mineralogist (MSA)
Cite as Authors (Year) Title. American Mineralogist, in press.
DOI: https://doi.org/10.2138/am-2019-6963

REVISION 1

Intra-eruptive trachyte-phonolite transition: natural evidences and experimental constraints on the role of crystal mushes

Marco Brenna[1]*, Alessio Pontesilli[1], Silvio Mollo[2], Matteo Masotta[3], Shane J. Cronin[4], Ian E.M. Smith[4], Mohammed Rashad Hassan Moufti[5], Piergiorgio Scarlato[6]

[1] Geology Department, University of Otago, Dunedin, New Zealand

[2] Dipartimento di Scienze della Terra, Sapienza Università di Roma, Rome, Italy

[3] Dipartimento di Scienze della Terra, Università di Pisa, Pisa, Italy

[4] School of Environment, University of Auckland, Auckland, New Zealand

[5] Faculty of Earth Sciences, King Abdulaziz University, Jeddah, Saudi Arabia

[6] Istituto Nazionale di Geofisica e Vulcanologia, Roma, Italy

* corresponding author: marco.brenna@otago.ac.nz

ABSTRACT

The generation of silica undersaturated phonolite from silica saturated trachytes is uncommon, as it implies the crossing of the thermal barrier and critical plane of silica undersaturation. Nevertheless, a co-genetic suite displaying compositional transition from benmoreite-trachyte to phonolite has been observed within the Al Shaatha pyroclastic sequence in the Harrat Rahat Volcanic Field (Kingdom of Saudi Arabia). We performed crystallization experiments on benmoreite and trachyte starting compositions in order to simulate the pressure-temperature-volatile conditions that generated the observed liquid line of descent. The experimental conditions were 200-500 MPa, 850-1,150 °C, 0-10 wt.% H_2O, 0.0-0.5 wt.% CO_2 and NNO+2 oxygen buffer. The experimental mineral assemblage consists

of clinopyroxene, feldspar and titanomagnetite, as well as glass in variable proportions. The degree of crystallinity of hydrous runs is lower than that of anhydrous ones at analogous pressure and temperature conditions. Clinopyroxene crystallizes with compositions diopside-augite and augite-hedenbergite, respectively at 500 MPa and 200 MPa. The saturation of feldspar is primarily controlled by temperature and volatile content, with the more potassic composition equilibrating at low temperature (850-900 °C) and anhydrous (for benmoreite) or hydrous (for trachyte) conditions. At low pressure (200 MPa), temperatures below 850 °C and anhydrous conditions, the degree of crystallization is extremely high (>90%) and the residual glass obtained from trachyte experiments is characterized by peralkaline and sodic affinity. This finding is consistent with natural eruptive products containing interstitial phonolitic glass within an anorthoclase framework. The shift from trachyte to phonolite is therefore interpreted as the result of open system interaction between trachytic magma and intercumulus phonolitic melt, as well as of dissolution of anorthoclase from a crystal mush.

Keywords: trachyte, phonolite, crystallization experiments, intercumulus melt, crystal mush

INTRODUCTION

Phonolites are silica undersaturated alkaline rocks characterized by a higher alkali content than trachytes. In intraplate volcanic settings, trachytes and phonolites are frequently associated within the same volcanic system, although phonolites are less abundant (Coombs et al., 2008; LeMasurier et al., 2011) and traditionally interpreted as the magmatic evolution of silica undersaturated primary basanitic magmas (Ablay et al., 1998; Coombs and Wilkinson, 1969; Kyle et al., 1992; Thompson et al., 2001; Wiesmaier et al., 2011; Wörner

and Schmincke, 1984). In contrast, the generation of trachytes is often attributed to the magmatic evolution of Si-rich alkaline basalts (Brenna et al., 2012; Brenna et al., 2015; Coombs and Wilkinson, 1969; Davidson and Wilson, 1989; Kim et al., 2018; Martel et al., 2013; Thompson et al., 2001; White et al., 2012). Additional magmatic transitions may occur with general divergences from trachytes towards phonolites or peralkaline rhyolites (Ackerman et al., 2015; Azzouni-Sekkal et al., 2007; Legendre et al., 2005; Upton, 1974). In this context, rhyolites are interpreted to derive by low pressure (<200 MPa) fractionation of trachytic magmas (LeMasurier et al., 2011; Romano et al., 2018), whereas the transition from trachytes to phonolites is less clearly defined due to a variety of pressure-dependent differentiation mechanisms involving variable mineral assemblages. For example, phonolites from the Teide–Pico Viejo stratovolcano (Canary Islands; Andújar and Scaillet, 2012), Laacher See volcano (Germany; Harms et al., 2004), as well as caldera systems at Suswa volcano (White et al., 2012), Ischia (Brown et al., 2014) and Campi Flegrei (Italy; Forni et al., 2016), are modelled to derive through interaction of crystal mushes and magma recharge in shallow crustal (<200 MPa) reservoirs. In the Marie Byrd Land volcanic province (Antarctica), LeMasurier et al. (2011) interpreted the origin of phonolites as the effect of crystal fractionation from trachytic melts stored at intermediate (~300 MPa) pressures. At Ulleung Island (South Korea), Brenna et al. (2014) attributed the formation of phonolites to high pressure (~1 GPa) differentiation mechanisms at the base of the crust. More complex models also invoke crustal contamination/assimilation phenomena as well as potential crustal melting for the generation of diverging trends at the silicic end of the alkaline series (Freda et al., 2008; Kyle et al., 1992; Legendre et al., 2005). Nonetheless, phonolitic eruptions are also known to host peridotitic xenoliths from the upper mantle (Irving and Price, 1981), suggesting deep magma derivation and no crustal interaction. Mixing of shallow-stalled

phonolitic melts with mantle-derived xenolith-hosting primitive melts may also explain the occurrence of peridotite xenoliths (Grant et al., 2013).

Phonolites occur in both composite volcanoes (e.g. Teide, Vesuvius, Ulleung) as well as in magmatic systems that lack a focused plumbing system and hence produce dispersed eruptive centres (e.g. East Eifel, Hoggar, Waipiata volcanic fields). These latter systems differ from composite volcanoes in that they have lower magma flux and hence a less sustained plumbing system (Valentine and Gregg, 2008). As a consequence, the dynamics of magma storage and evolution in volcanoes with dispersed plumbing will differ from those of long-lived crustal systems due to the lower recharge rates and thermal budgets (Cioni et al., 1998; Di Renzo et al., 2016; Ginibre et al., 2004). Because of the lack of mature multistage storage that may obfuscate evolutionary processes, "monogenetic" silicic alkaline eruptions displaying compositional change from trachyte to phonolite provide an opportunity to investigate the magmatic mechanism controlling the transition. Such eruptions are ideal due to their restricted temporal and spatial association, implying chemical transition within a single erupted magma batch, potentially derived from shallow amalgamation of several magma pulses.

The trachyte-phonolite association is found in the tephras of the Al Shaatha pyroclastic flow sequence in the Harrat Rahat Volcanic Field (Kingdom of Saudi Arabia; Moufti et al., 2012; Stelten et al., 2018). In this study, we used an experimental approach to investigate the phase relationships of benmoreite and trachytes forming the Al Shaatha eruptive sequence. These experimental results allow to elucidate the P-T-H_2O-CO_2 conditions controlling mineral crystallization and magma differentiation, with potential implications for the origin of phonolitic melts in dispersed magmatic settings, such as in the Harrat Rahat Volcanic Field.

GEOLOGICAL SETTING

The Harrat Rahat Volcanic Field (hereafter HRVF) is situated south of the city of Al-Madinah and belongs to a series of lava-dominated volcanic fields aligned sub-parallel to the east coast of the Red Sea and generated in response to the asymmetric rifting there (Fig. 1a) (Bohannon et al., 1989). Volcanism in the area has been active over the past 10 Ma (Moufti et al., 2013), with two monogenetic basaltic eruptions in historic times impacting, with lava flows and tephra fallout, the city of Al-Madinah in 641 and 1256 AD (Fig. 1b; Camp and Roobol, 1989). Lavas in the HRVF vary from alkaline basalt to trachyte with minor intermediate compositions (Moufti et al., 2012; Stelten et al., 2018). They were erupted along with Hawaiian and Strombolian events forming over 950 scoria and spatter cones (exposed) over the lifetime of the field (Camp et al., 1987; Murcia et al., 2014; Runge et al., 2014). Pleistocene trachytic eruptions (~0.1-0.5 Ma) extend over an area of ~20-30 km southeast of the city of Al Madinah (Fig. 1b; Moufti et al., 2013). The more evolved eruptive products are lava domes, tephra and pyroclastic sequences. Magmatic evolution from basaltic parent melts towards the differentiated terms occurred principally through fractional crystallization with minor crustal assimilation (Moufti et al., 2012), and is estimated to have lasted ~10-25 kyr (Stelten et al., 2018).

Al Shaatha is an overall trachytic pyroclastic complex with minor benmoreite and phonolite. It is situated to the northwest of the larger Al Efairia volcanic centre (Fig. 1b; Moufti and Németh, 2016). The pyroclastic apron covers a pre-existing basaltic volcanic structure (Fig. 1c), with the subtle 500 m wide crater rising ~100 m above the surrounding landscape. The

block-and-ash flow sequence is best exposed to the west of the crater area where a wadi incised the sequence. SH05 was a section that contained the most complete sequence as described in the Electronic Appendix A. The sequence comprises a stack of thick ashy-matrix supported breccias with coarse dominantly trachytic pumice. Matrix comprises fragmented pumice of the same composition. These deposits contain few (<5%) lithics, mainly basaltic country rock. These are deposits consistent with particle-rich or dense pyroclastic density current (PDC) deposits. The coarse matrix supported pyroclastic breccias are intercalated with finer-grained, poorly sorted lapilli tuffs, with cross bedding indicative of dilute PDCs. The bedded, units contain a greater content of country rock materials (<20% by volume) which is mainly basaltic scoria or lava), but are dominated by similar trachytic high-density pumice. The base of the sequence contains a clast-supported lapilli unit, indicative of a tephra fall. This contains up to 60% country rock fragments of basaltic scoria or lava fragments.

Sharp contacts between units and coarse/thick pyroclastic density currents intercalated with multiply bedded finer grained PDC deposits indicates that the eruption involved a complex sequence of collapses from unstable eruption columns. No evidence for weathering or non-volcanic erosion occurs between deposition units, so that the sequence was emplaced over one extended episode. Some deposits cut into others and pinching and swelling of unit thicknesses in association with topography is consistent with laterally moving currents interacting with topography. Welding, where present, crosses several stratigraphic/depositional boundaries, which is also consistent with a short eruption duration, particularly for the upper half of the sequence.

The primary pyroclastic textures of these materials are similar dense vesiculated and microcrystalline trachytes, with increasing porosity from base to the top of the sequence. The

uppermost unit is the most widespread and contains many bread-crusted and cauliflower bomb textures. The eruption sequence is envisaged as the unroofing/disruption of a strongly degassed crystalline magma cap, before successive eruption of gas-rich, lower viscosity magma below. The high crystal content meant that vesicle growth was hindered by the crystal network and deformed vesicles are ubiquitous. The eruption began with a stable phase, producing lithic-rich tephra fall as the vent system established. The eruption never reached a stable sub-Plinian state, and instead repeated collapse occurred – or a series of low-energy boiling-over columns (Kano et al., 1997; Shea et al., 2011), likely due to low rates of magma expansion. The final phase was the most energetic, producing PDCs that reached 3 km from the vent, associated with the highest vesicularities.

We collected juvenile clasts consisting of lapilli and bombs within each of the main pyroclastic flow units in a comprehensive stratigraphic section representative of the entire eruptive sequence (Electronic Appendix A). We additionally sampled distal and medial deposits (Fig. 1c), and their compositional variations are described below.

ANALYTICAL AND EXPERIMENTAL PROCEDURES

Whole rock analyses

Whole rock major element analyses (Table 1) were performed at the School of Environment, University of Auckland (New Zealand) by X-ray fluorescence (Siemens SR3000 spectrometer). Organic material was removed by sample washing, i.e., soaking in a hot mixture of HCl and H_2O_2 and cleaning in acetone using ultrasound. Loss-on-ignition (LOI) was calculated by heating ~4 g of sample for 12 hours at 105 ºC and 1,000 ºC, respectively. Then, 2 g of dried sample powder were mixed with 6 g of SPECTRACHEM 12-22 flux. The

mixture was fused in a Pt crucible to obtain a homogeneous glassy bead. The oxide components were measured following Norrish & Hutton (1969), with precision better than ±1% (1σ). The Compton scatter of X-ray tube RhKb1 emission was used to correct for mass attenuation. Theoretical detection limit is 1-2 ppm and reproducibility is <5% (2σ).

Microchemical analyses

Microchemical data (Electronic Appendix B) were acquired with an electron probe microanalyzer (EPMA) using a JEOL JXA 8200 with combined EDS-WDS (five spectrometers with twelve crystals) installed at the HP-HT Laboratory of Experimental Volcanology and Geophysics of the Istituto Nazionale di Geofisica e Vulcanologia (INGV) in Rome, Italy. The accelerating voltage and beam current were 15 kV and 10 nA, respectively. The beam size was 5 μm (glass analyses) and 1 μm (mineral analyses) with a counting time of 20 and 10 s on peaks and background, respectively. The following standards have been adopted for the various chemical elements: jadeite (Si and Na), corundum (Al), augite (Ca), forsterite (Mg), andradite (Fe), rutile (Ti), orthoclase (K), barite (Ba), apatite (P) and spessartine (Mn). Sodium and potassium were analysed first to prevent alkali migration effects. The precision of the microprobe was measured through the analysis of well-characterised synthetic oxides and minerals. Data quality was ensured by analysing these test materials as unknowns according to Iezzi et al. (2014). On the basis of counting statistics, analytical uncertainties relative to their reported concentrations indicate that precision was better than 5% for all cations analysed.

Crystallization experiments

Crystallization experiments were conducted at the HP-HT Laboratory of the INGV Rome. The starting materials consist of a benmoreite and a trachyte (samples SH1A as SMA and

SH5C as SMB, respectively; Table 1) from the Al Shaatha eruptive centre, selected as representative of the parental and intermediate compositions of the eruptive sequence (Fig. 2a). We opted to perform experiments only using the erupted magma compositions rather than a hypothetical basaltic parent, because these magma compositions represent the point of interest for the investigation of the transition from trachyte to phonolite. The starting materials were melted in a Fe-presaturated Pt-crucible at 1,200 °C for 30 min in a vertical tube CO–CO_2 gas-mixing furnace at the NNO+2 oxygen buffer. The microchemical analyses of the glasses did not reveal the presence of crystalline phases, yielding homogeneous compositions comparable to the whole rock analyses (Table 1). Piston cylinder experiments (Table 2) were carried out using a non-end loaded apparatus ("QUICKpress", Depths of the Earth co.) using a 19-25 mm NaCl-borosilicate glass-graphite-MgO assembly producing a redox state close to the NNO+2 oxygen buffer (Masotta et al., 2012). The assembly was simultaneously loaded with two AuPd-capsules containing the starting materials. The crystallization experiments were conducted under either anhydrous or H_2O- and CO_2-bearing conditions. For the nominally anhydrous experiments, the powdered starting materials were dried in an oven at 110 °C for 48 h. For the volatile-bearing experiments, deionized H_2O was added with a microsyringe to the starting materials or, alternatively, CO_2 was added in the form of Ag_2CO_3 powder. After sealing, capsules were heated to 105 °C for 30 minutes and none had weight loss due to volatilization. The benmoreite crystallization experiments (Experimental Set A) were conducted at 200-500 MPa representative of shallow and mid crustal storage, 850-1,150 °C, anhydrous to 4.0-10.1 wt.% H_2O, and 0.25-0.5 wt.% CO_2. Conversely, the trachyte crystallization experiments (Experimental Set B) were conducted at 200-500 MPa, 850-1,000 °C, anhydrous to 4.6-7.1 wt.% H_2O, and 0.31 wt.% CO_2. The AuPd-capsules placed in the assembly were surrounded by powdered pyrophyllite to prevent H_2O loss and enhance stress homogenization during initial compression (Freda et al., 2001;

Freda et al., 2008). After cold pressurization to a nominal pressure 10% higher than that desired, the pressure was decreased down to the target value and maintained constant for the duration of the experiment. Experiments were carried out by heating the starting glass from room temperature to the superliquidus condition of 1,200 °C. Note that the anhydrous liquidus temperature is 1,190 °C and 1,179 °C for the benmoreite and trachyte, respectively, as derived by the MELTS code (Ghiorso and Gualda, 2015; Gualda et al., 2012). The temperature was kept constant at superliquidus for 30 min and then decreased at the rate of 80 °C/min down to the target temperature. The temperature was monitored by a factory-calibrated K-type (chromel-alumel) thermocouple with uncertainty of ±3 °C. In order to guarantee the achievement of equilibrium crystallization conditions in benmoreitic and trachytic melts, the experimental time duration was comprised between 24 and 70 h (cf. Masotta et al., 2013). The experiments were isobarically quenched at the rate of 100 °C/s.

CHEMOSTRATIGRAPHIC SEQUENCE OF THE AL SHAATHA ERUPTION

The eruption forming the Al Shaatha pyroclastic sequence started with a relatively evolved (SiO_2-rich) trachyte and phonolite, and transitioned to a less evolved (SiO_2-poor) benmoreite emplaced at the top of the eruptive sequence (Table 1, Fig. 2). From bottom to top in the stratigraphy, SiO_2, Al_2O_3 and K_2O decrease, whilst TiO_2, FeO_{tot}, MgO, CaO and P_2O_5 increase. The Na_2O remains overall constant or increases weakly up stratigraphy, apart for two phonolitic rocks close to the base of the sequence (Fig. 2a, h). Although minor variability may be present within each unit, major heterogeneities are unlikely because the composition of the top unit at location SH5 (SH5J) is equivalent to that of SH1A, which is its distal equivalent.

The eruptive products range from poorly vesicular (<25%) and crystalline (diktytaxitic texture; groundmass microlites protrude into vesicles and form their walls) trachyte and phonolite at the base of the eruptive sequence, to highly vesicular (>60%) (and diktytaxitic) benmoreite at the top (Fig. 3). Flow textures are well developed in both trachytes and phonolites (Fig. 3b, c). All samples contain <5% microphenocrysts (0.5-1 mm) of feldspar, green (under plane polarized light) hedenbergitic clinopyroxene, fayalitic olivine and magnetite to titanomagnetite in an aphanitic (<0.2 mm) groundmass of feldspar + hedenbergitic clinopyroxene + titanomagnetite. Mineral analyses are reported in Electronic Appendix B. Olivine (Fo_{18-24}) crystals are euhedral and fresh in the benmoreite, whereas they are variably altered to iddingsite in trachyte and phonolite (Fig. 3a, b). Clinopyroxene microphenocrysts in the benmoreite have variable composition $Wo_{43-49}En_{12-26}Fs_{30-41}$, whereas in the trachyte and phonolite the mineral composition is more restricted to $Wo_{45-48}En_{7-11}Fs_{43-46}$ (Fig. 4 and Elecronic Appendix A). Minimal zonation is present in clinopyroxene microphenocrysts (Fig. 3e) where rims have FeO slightly higher than in cores, and comparable to groundmass clinopyroxene. Feldspar microphenocrysts are mostly oligoclase ($An_{10-25}Ab_{70-80}Or_{10-20}$) in the benmoreite and anorthoclase in trachyte and phonolite ($An_{<10}Ab_{50-80}Or_{15-55}$; Fig. 5 and Electronic Appendix B) and show no or only minor zonation. The phonolite contains also glomerocrysts of unzoned, sieve-textured anorthoclase and minor hedenbergitic clinopyroxene, analogous in composition to those in the trachyte and phonolite groundmass (Fig. 3d, f). Titanomagnetite is often associated with the mafic microphenocrysts (Fig. 3a, b, c). The benmoreite contains the most titaniferous magnetite with 12 to 18 wt.% TiO_2, whereas magnetite has TiO_2 varying from 1 to 6 wt.% in the trachyte. Titanomagnetite composition in the phonolite is similar to that of crystals in the benmoreite (Electronic Appendix B). Zircon and apatite occur as rare accessory mineral phases.

EXPERIMENTAL RESULTS

Anhydrous and hydrous experiments were performed at 850-1,150 °C and 200-500 MPa, producing variable proportions of clinopyroxene, feldspar, titanomagnetite and glass, with trace amounts of apatite. None of the experiments crystallized fayalitic olivine.

Phase assemblage and texture

Back-scattered images of representative run products from Experimental Set A (Fig. 6a, b, c) and Experimental Set B (Fig. 6d, e, f) show that crystals are generally euhedral with well-developed faces. Titanomagnetite and glass are ubiquitous in the phase assemblage whereas clinopyroxene and feldspar are present in variable proportions. Feldspar crystallization is supressed at 1,000-1,150 °C and 10.1 wt.% H_2O in experimental set A (Table 2). Experiments performed at 200 MPa exhibit identical phase assemblages, with the fraction of residual melt increasing at hydrous conditions (Fig. 7a). Volatile saturation in hydrous experiments is testified by the presence of vesicles (<5%). The crystallization of feldspar increases remarkably at anhydrous conditions, particularly in the trachyte (Experimental Set B; Fig. 7b). In contrast, at both hydrous and anhydrous conditions, experiments performed with the benmoreite (Experimental Set A) exhibit larger proportions of clinopyroxene (Fig. 7b). Overall, in the temperature range 850-1,000 ºC, the effect of H_2O in decreasing the degree of crystallization prevails over that of temperature (cf. Run# A3 vs. A10, Run# A22 vs. A25, Run# B1b vs. B2, and Run# B3 vs. B4; Table 2). At 850 ºC, the experimental charges are almost completely crystallized, with the exception of minor glassy pockets (Fig. 6 c, f).

A pressure of 500 MPa subdues both the plagioclase and clinopyroxene saturation surfaces, resulting in more abundant residual glass compared to anhydrous 200 MPa conditions (cf. Run# A21 vs. A25, Run# B1 vs. B2, and Run# B5 vs. B10; Fig. 7a; Table 2). The phase assemblage does not change considerably in CO_2-bearing and CO_2-absent experiments (cf. Run# A23 vs. A26, and Run# B5 vs. B6, Table 2), denoting a negligible effect of CO_2 on the crystallization behaviour. Traces of apatite are also observed in experiments conducted at 850-950 ºC, when modal crystallinity is >50%.

Mineral chemistry

In both Experimental Set A (benmoreite) and Experimental Set B (trachyte), clinopyroxene crystals formed at 500 MPa under either anhydrous or hydrous conditions and exhibits compositions that differ from those of the natural samples, resulting enriched in MgO, Al_2O_3 and TiO_2 (Fig. 4; Electronic Appendix B). The best matching with the natural clinopyroxene is obtained in the benmoreite at 200 MPa and 850-950 °C, under both hydrous (Run# A4 and A5) and anhydrous (Run# A15 and A22) conditions. This clinopyroxene is less calcic than that formed at 1,000-1,150 °C, thus resembling the natural MgO-poor phenocrysts. In turn, at 1,000-1,150 °C the composition of clinopyroxene obtained at 200 and 500 MPa does not substantially change. Clinopyroxenes crystallized from the trachytic melt are remarkably enriched in MgO with respect to those from natural products. However, at 200 MPa and 850 °C (Run# B8), the experimental crystals obtained under anhydrous conditions closely reproduce the natural phenocryst compositions.

In the experiments with the benmoreite, feldspars obtained under anhydrous conditions display an increase of Or component from $An_{28}Ab_{63}Or_8$ to $An_6Ab_{60}Or_{34,}$ with decreasing

pressure and temperature (cf. Run# A23 vs. A5). The compositional variability of feldspar in experiments conducted at 500 MPa does not match with that of natural feldspars in the benmoreite, particularly for the different Ab content (Fig. 5; Electronic Appendix B). At 200 MPa, the addition of H_2O causes a marked decrease in Or component, with most feldspars from hydrous experiments having composition $An_{20-27}Ab_{65-70}Or_{6-10}$. The best overlap is observed at 200 MPa, 900 °C and 4 wt.% H_2O (Run# A15) where feldspar composition ranges from oligoclase to anorthoclase. The Al_2O_3 content and Na_2O/K_2O ratio of experimental crystals are also analogous to those of feldspars in the natural benmoreite.

In the experiments with the trachyte, most of the feldspars have compositions $An_{3-17}Ab_{63-70}Or_{21-38}$, in good agreement with natural samples. At 500 MPa, the experimental crystals cluster towards the Or-poor terms of the natural spectrum (Fig. 5). H_2O-bearing experiments at $T \leq 950$ °C (Run# B3 and B7) have Or component higher than CO_2-bearing experiments at $T \geq 1{,}000$ °C (Run# B6) (Fig. 5). Hydrous experiments at $T \leq 950$ °C and 200 MPa (Run# B3 and B7) with feldspar compositions of $An_{1-5}Ab_{55-59}Or_{36-44}$ show the best overlap with Or-rich data from natural crystals (Fig. 5).

Titanomagnetite crystals from Experimental Set A and Experimental Set B have TiO_2 abundance of less than 10 wt.%, being thus quite different from the titaniferous magnetites naturally occurring in the benmoreite (Electronic Appendix B). TiO_2 abundance generally decreases at 500 MPa and anhydrous conditions. Only the experimental crystals obtained at 200 MPa, 850-900 °C and 4.0- 4.6 wt.% H_2O (Run# A15 and B7) approach the crystals hosted in natural trachyte.

Glass chemistry

The Experimental Set A was designed to reproduce the magmatic evolution from benmoreite to trachyte using the benmoreite as starting composition (sample SH5C; Fig. 2a). The experimental glasses evolve from the initial benmoreite depicting decreasing trajectories for FeO, MgO, CaO, Al_2O_3, and P_2O_5, as well as increasing $Na_2O + K_2O$ trajectories at increasing SiO_2. Al_2O_3 and Na_2O show an inflection at ~65 wt.% SiO_2 (Fig. 8a, b). At hydrous conditions, experiments performed at 200 MPa are characterized by lower SiO_2 enrichments than at 500 MPa, irrespective of the temperature (Fig. 8). The general increase in SiO_2 results into lower enrichment of $Na_2O + K_2O$ and Al_2O_3, and lower depletion in TiO_2 compared to the Al Shaatha sequence (Fig. 8a, b, d). In the experimental glasses the Al_2O_3/CaO ratio diverges from the natural sequence (Fig. 8b), and FeO records a strong depletion vs. MgO compared to the natural samples (Fig. 8c). Nonetheless, anhydrous experiments performed at 200-500 MPa, as well as the hydrous experiment conducted at 200 MPa, 850 °C and 7.7 wt.% H_2O (Run# A21) exhibit enrichment of $Na_2O + K_2O$ and depletion of TiO_2 that closely resemble the natural sequence (Fig. 8a, d). At 500 MPa, 1,150 °C and anhydrous conditions (Run# A14) there is the best matching between experimental glasses and the chemical transition between benmoreite and trachyte.

The Experimental Set B aimed to reproduce the chemical variability to phonolite observed in the natural samples. At 200 and 500 MPa, the experimental glasses display broadly decreasing FeO, CaO, Al_2O_3, and Na_2O concentrations, in concert with broadly increasing K_2O contents as SiO_2 increases. The concentration of P_2O_5 and MgO remains relatively constant. The anhydrous glasses have Al_2O_3 concentrations lower than those measured for volatile-bearing experiments. At 500 MPa, the hydrous glass compositions record a strong depletion of $Na_2O + K_2O$ with respect to the starting material, whereas less effective

depletions are observed at 200 MPa (Fig. 9a, c). The glasses resulting from the Experimental Set B have a more restricted SiO_2 (63-68 wt.%) variability compared to those (58-71 wt.% SiO_2) from the Experimental Set A. However, because of the overall enrichment in SiO_2, none of the experiments produced glasses with phonolitic compositions. Moreover, the hydrous experiments exhibit the greatest deviation from the natural whole rock analyses. At 500 MPa and 1,000-1,150 °C, the anhydrous experiments are characterized by a mild enrichment of $Na_2O + K_2O$. In contrast, a more marked alkali enrichment is documented at 200 MPa and 850-950 °C (Run# B2 and B8). These glasses preserve a relative high abundance of MgO and FeO, and a high Al_2O_3/CaO ratio, pointing towards the compositions of natural phonolites (Fig. 9). The run products from Experimental Set A and Experimental Set B that better reproduce the parageneses of natural rocks are discussed in the next section (Fig. 10).

DISCUSSION

Magmatic evolution of the Al Shaatha eruptive sequence

The rationale behind the experiments conducted on the Al Shaatha sequence was to elucidate the magmatic conditions responsible for the origin of a phonolitic melt. Relative to the different mechanisms that were proposed for the generation of phonolites, the role of crustal partial melting (Hay and Wendlandt, 1995; Legendre et al., 2005) is improbable due to the limited volumes of magmas feeding the eruptions. Direct melting of lithospheric mantle (Laporte et al., 2014) is also excluded by the lack of xenocrysts/xenoliths suggestive of direct magma ascent from mantle depths. On the other hand, crystal fractionation is a commonly

advocated mechanism for the generation of phonolite from alkaline parent melts (Andújar and Scaillet, 2012; Brenna et al., 2014; LeMasurier et al., 2011; Wörner and Schmincke, 1984). At Al Shaatha, the volcano formed through a single eruptive sequence displaying the transition from benmoreite to trachyte and phonolite. This is not associated to the construction of a composite volcanic edifice deriving from a sustained magmatic plumbing system, and it is therefore unlikely that crustal contamination played a major role. Therefore, experiments from this study were designed to reproduce a phonolitic residual melt through crystallization of benmoreitic and trachytic magmas.

Despite the broad range of *P*-*T*-H_2O-CO_2 conditions explored by the crystallization experiments, none of the glasses obtained have *sensu stricto* phonolitic compositions. Only some experimental data describe quite well the compositions of natural minerals and whole rocks belonging to the benmoreite-trachyte geochemical transition. For the Experimental Set A (benmoreite), the glass compositions derived at 500 MPa and 1,150 °C under anhydrous conditions (Run# A14) better reproduce the natural variation of benmoreite to trachytes. Similarly, at 200 MPa and 850-900 °C under hydrous conditions (Run# A15 and A21), the experimental products reproduce the whole rock and microphenocryst (feldspar + clinopyroxene) compositions of the natural benmoreite. The experiments do not crystallize fayalitic olivine despite its stability (euhedral microphenocrysts without resorption features) in the natural benmoreite to trachyte at Al Shaatha, similar to other trachytic sequences (Macdonald et al., 2011). To test its absence, we have performed thermodynamic simulations using the rhyolite-MELTS code (v.1.2.0) (Gualda et al., 2012) based on the detection of phase saturation and energy convergence by Gibbs free energy minimization. These simulations were conducted at 500 MPa, 1,000-800 °C, 5 wt.% H_2O and buffering conditions variable from NNO to NNO+2.2. The benmoreitic melt was used as starting composition and

differentiated by a step-by-step crystal fractionation processes in which the temperature was lowered each 20 °C, leading to a maximum degree of solid fraction of 55 wt.%. Results from calculations indicate that, irrespective of the redox state of the melt, clinopyroxene is the liquidus phase followed by oxide. However, the formation of fayalitic olivine (Fo_{83-87}) is relegated to a low-temperature (800-860 °C) crystallization path when the system has already fractionated 20 wt.% of minerals and the buffering condition is close to NNO. The degree of olivine fractionation is also extremely low (1-5 wt.%) and basically ineffective during the differentiation of the less oxidized melt.

Anhydrous experiments at low temperature exhibit SiO_2 enrichments higher than those measured in the volatile-bearing products (cf. Run# A4 vs. Run# A20 and A21), with residual melt compositions departing from the phonolite field. In the Experimental Set B (trachyte), only experiments performed at low *P*-*T* conditions apparently reproduce the whole rock and mineral compositions observed in the natural samples. The composition of the residual melts in equilibrium with clinopyroxene and feldspar matches with that of Al Shaatha trachytes at 200 MPa, 850 °C and anhydrous conditions (Run# B8). These coupled findings from Experimental Sets A and B seem to corroborate a scenario where the overall anhydrous melt crystallized at multiple depths. The benmoreite to trachyte transition likely occurred during ascent from mid- to shallow-crustal levels with the formation of a phonolite melt occurring at relatively shallow levels.

Although none of the experiments reproduced in full the whole rock analyses of phonolites, some experimental glasses show chemical characteristics indicative of a shift towards phonolitic affinity. For instance, in volatile-bearing experiments performed with the trachyte and equilibrated at 200 MPa and 850 °C (Run# A20 and partly A21), the residual glasses

449 display an increase of the Na_2O/K_2O ratio from 1.8 to 4.5, which is consistent to what
450 observed for the Al Shaatha phonolites. These experimental products are strongly crystalline
451 with a low fraction of interstitial glass (less than 2%) and diktytaxitic vesicularity (Fig. 6c).
452 In comparison, experiments performed with the benmoreite at 200 MPa, 850-900°C and
453 anhydrous conditions (Run# B4 and B8), yield a high crystal content with scarce interstitial
454 glass (Fig. 6f). The residual glass composition results more enriched in $Na_2O + K_2O$ relative
455 to the less crystalline experiments gained at high *P*-*T*-H_2O conditions. This residual glass,
456 however, is dramatically enriched in SiO_2 with respect to natural phonolitic terms. It cannot
457 be excluded that the SiO_2 enrichment is caused by an enhanced stability of the clinopyroxene
458 + titanomagnetite assemblage in the experiments with respect to the crystallization of
459 magmas at Al Shaatha. It should be noted that the oxygen fugacity imposed by the piston
460 cylinder assembly (NNO+2 buffer) is almost comparable to that (from NNO+1 to NNO+2.3
461 buffer) documented for trachytes and phonolites from other volcanic settings (Berndt et al.,
462 2001; Fabbrizio and Carroll, 2008; Freise et al., 2003; Martel et al., 2013). This may have
463 been slightly lower in the benmoreite due to stability of fayalitic olivine. However,
464 iddingsitisation of fayalite in the trachyte and absence of fayalite in the phonolite likely
465 indicate a rise in oxygen fugacity (Caroff et al., 2000) comparable to experimental
466 parameters. Rationally, it is hypothesized that classical closed-system crystallization
467 mechanisms cannot be responsible for the overall geochemical evolution of magmas at Al
468 Shaatha, especially for the alkali-rich phonolites. In this context, we embrace some
469 perceptions reported in the recent review study of Bachmann and Huber (2016) and
470 illustrating the role of crystalline region (i.e. mush zones) within the mid-to-shallow crustal
471 reservoirs, on the chemical and dynamical evolution of the magmatic system (see discussion
472 and model below).
473

474 **Late-stage residual phonolitic melt**

475

476 One interesting observation from our crystallization experiments is the lack of glass
477 compositions analogue to the natural phonolites (*sensu stricto*) erupted at Al Shaatha. In this
478 regard, several early experimental works (Bailey and Schairer, 1964; Carmichael and
479 MacKenzie, 1963; Thompson and MacKenzie, 1967) demonstrated that silicic peralkaline
480 melts may evolve to more sodic compositions by abundant crystallization of alkaline
481 feldspar. We found that metaluminous melts become peralkaline at 200 MPa, showing a net
482 increase of the Na_2O content and directing the magmatic differentiation towards the
483 phonolitic terms of the Al Shaatha eruptive sequence. This compositional change is more
484 evident for the experiments performed with the trachyte (Experimental Set B), where the
485 crystallization is dominated by alkaline feldspar (anorthoclase) over clinopyroxene,
486 particularly at anhydrous conditions (Fig. 7b). Conversely, in the experiments performed with
487 the benmoreite (Experimental Set A), the residual melts do not gain a peralkaline affinity,
488 despite their compositions showing an increase in the sodic character (Fig. 10).

489

490 At Al Shaatha we exclude an origin of the trend toward peralkalinity and phonolite solely as
491 a result of the extraction of a feldspar cumulate. Alkaline feldspars in the trachyte have SiO_2
492 ~65 wt.% and approximately equal abundances of Na_2O and K_2O (~6-7 wt.%) (Electronic
493 Appendix B). The two natural samples evolving towards phonolite (which contain the
494 anorthoclase glomerocrysts) show an overall decrease of SiO_2 and increase of Na_2O over
495 K_2O compared to the trachyte. It is therefore unlikely that the shift is caused by accumulation
496 or incorporation of feldspar glomerocrysts alone. Nevertheless, it is possible that partial
497 resorption of anorthoclase from a crystal mush zone, as indicated by the sieve texture of

feldspars in the glomerocrysts (Fig. 3d) could have contributed to generation of phonolitic liquids, as previously suggested by Brown et al. (2014).

Trachytes and phonolites are rarely interpreted as cogenetic magmas originating from the same crystallization path, however, their intimate occurrence requires an explanation. Here we draw on several other occurrences where trachyte and phonolite are closely associated, with the aim to better understand the mechanisms that could generate such a transition. The Atakor Massif in the Hoggar volcanic province (Algeria) displays two clear diverging chemical trends from trachyte to rhyolite and from trachyte to phonolite (Azzouni-Sekkal et al., 2007). The volcanic products from the Kangerlussuaq Intrusion (Greenland) are interpreted as an open-system magma recharge event producing a trachyte-phonolite lineage by crystal fractionation from a basanitic parental magma (Riishuus et al., 2008). The last eruptive activity (~10-2.5 ka) at Ulleung Island (South Korea) formed a tephra sequence transitioning from trachytic to phonolitic compositions (Brenna et al., 2014; McLean et al., 2018 and references therein). Brenna et al. (2014) proposed that the late crystallization of plagioclase from the trachytic magma at lower crustal conditions caused SiO_2 depletion and $Na_2O + K_2O$ enrichment in the residual phonolitic melts. At Ulleung Island some cognate enclaves occur within the tephra representative of the trachyte-phonolite transition (Brenna et al., 2014). One of these cognate enclaves is a syenitic cumulate consisting of an intricate framework of alkaline feldspar and green sodic clinopyroxene, with also minor oxides and interstitial vesiculated glass. This interstitial glass has composition extending further into the phonolite field compared to the Al Shaatha eruptive sequence, thus suggesting melt extraction from a crystal-rich zone and further entrainment in the ascending magma (Hildreth and Wilson, 2007). Similar cognate enclaves largely consisting of alkaline feldspar (sanidinites) have been also observed in the eruptive deposits of the major phonolitic

eruptions of the Sabatini Volcanic District (central Italy) and interpreted as part of differentiated crystal mushes (Masotta et al., 2016). Complex crystallization and magma recharge events feeding trachytic/phonolitic magmatic reservoirs may lead to crystallization and resorption of selected mineral phases (e.g. anorthoclase), which could shift the melt composition between the two compositional fields (Brown et al., 2014; Ridolfi et al., 2006; White et al., 2012). Indeed, the development of a crystal mush is one of the most effective mechanisms controlling the textural and compositional variations of silicic products, such as trachytes and phonolites (Masotta et al., 2010). In this framework, the magmatic differentiation is intimately correlated to the interplay between crystal accumulation and melt extraction (Bachmann and Bergantz, 2004; Dufek and Bachmann, 2010; Huber et al., 2009), where crystal-rich enclaves testify to the solid residual of the crystal-melt separation processes (Forni et al., 2016; Forni et al., 2018; Masotta et al., 2016).

In the case of Al Shaatha eruptions, several glomerocrysts and/or cognate microenclaves of anorthoclase and hedenbergitic clinopyroxene occur in the phonolitic tephra (Fig. 3d). Because of the limited eruptive volume and history, these glomerocrysts may represent disrupted portions of a crystal mush related to earlier stalled intrusions, rather than major crustal reservoirs like in classical large caldera systems (Fig. 11). Interstitial phonolitic melts originated in such a relatively short-lived reservoir and eventually interacted with benmoreitic/trachytic melts at shallow crustal levels (Fig. 11) (Dufek and Bachmann, 2010; Thompson et al., 2001). We tested this hypothesis by mass balance calculations performed with the Petrograph software (Petrelli et al., 2005) and based on least-square modelling equations of Stormer and Nicholls (1978). Using as input parameters major oxide analyses of natural samples and experimental phases (Table 3), the model successfully reproduces the variation from the trachyte SH5C (i.e., the starting material of Experimental Set B) to the

548 phonolite SH5E. This model does not imply that a liquid reservoir formed with phonolite
549 composition, but simply simulates the composition of a residual interstitial melt following
550 extensive crystallization. The overall amount of crystallization necessary to generate the
551 phonolitic melt is ~80%, with modal abundances of 89% K-feldspar, 6% clinopyroxene and
552 5% oxide (Table 3). This compositional variation is consistent with the experimental glass
553 obtained at 200 MPa, 850 °C and anhydrous conditions, in response to abundant
554 crystallization (Run# A20 and A21; Table 2). The sum of the squared residuals (SSR) yields
555 a reliable value of 0.44, making the modelling results realistic for the Al Shaatha eruptive
556 sequence. It can be thus concluded that the formation of materials with phonolitic affinities
557 may be related to the development of a crystal mush and further crystal-melt separation
558 mechanisms (Bachmann and Bergantz, 2004). Coherently, other authors (Caroff et al., 1997;
559 Panter et al., 1997) have effectively demonstrated as the fractionation of clinopyroxene and
560 abundant feldspar from alkaline basalts/basanites may produce ~20% of residual phonolitic
561 magmas, in close agreement with the melt proportion obtained in this study (Table 3).
562
563
564 **IMPLICATIONS**
565
566 The peralkaline and sodic character of Al Shaatha eruptive products testifies to complex
567 mechanisms of magma differentiation that determine the transition from SiO_2-saturated
568 trachytes to SiO_2-undersaturated phonolites. To better understand the mechanisms behind this
569 transition, we have performed crystallization experiments at mid- and upper-crustal pressures
570 and temperature and a range of volatile conditions, using as starting materials benmoreitic
571 and trachytic rocks from the Al Shaatha pyroclastic sequence in the Harrat Rahat Volcanic
572 Field (Kingdom of Saudi Arabia). The experimental results suggest that, at 500 MPa and

1,000-1,150 °C, the Al Shaatha benmoreitic magma differentiated towards trachytic compositions through crystallization of clinopyroxene, feldspar (oligoclase) and titanomagnetite. Experiments conducted at 200 MPa and 950-850 °C suggest that the formation of trachytic magmas continues at shallower crustal levels and lower temperatures. Although none of the investigated experimental conditions reproduced the alkali increase coupled with a decrease or unchanged SiO_2, the overall peralkaline and sodic character of the experimental glasses increases at low-P and low-T, analogously to the natural transition from trachyte to phonolite. The inconsistency between natural and experimental data suggest that the SiO_2-undersaturated phonolitic magmas constituting the Al Shaatha pyroclastic sequence originated at open-system-like conditions through crystallization of anorthoclase from an initially SiO_2-saturated trachytic liquid. Crystallization of an alkali feldspar-dominated phase assemblage is supported by the occurrence of glomerocrysts constituted in the largest part by anorthoclase (Fig. 3d), although the mass balance calculations indicate a high amount of crystallization (80%). This could potentially lock up the melt within the crystal mush (Deering et al., 2011). However, physical disturbance by later injections could generate melt channels within the mush like what has been documented and modelled to occur within the mantle to mobilize very low degrees of partial melts (Katz et al., 2006). A complex interplay of crystallization, anorthoclase resorption, melt segregation and mixing occurring through a vertically developed mush pile could determine the transition from trachytic to phonolitic magma compositions. In this scenario, the highly crystalline portion of the shallower intrusion is interpreted to evolve into a crystal-rich mush zone, from which interstitial melts with a strong phonolitic affinity are progressively extracted and, to variable extent, interact with trachytic magmas (Fig. 11).

ACKNOWLEDGEMENTS

598 This project was supported by a University of Otago Research Grant (UORG) to MB. King
599 Abdulaziz University and the University of Auckland supported field and sampling costs
600 through the VORISA project. Manuela Nazzari provided helpful assistance with EPMA
601 analyses at INGV Rome. We thank Katy Chamberlain and an anonymous reviewer for
602 constructive comments and Dan Morgan for editorial handling.
603

604 **References**

605 Ablay, G.J., Carroll, M.R., Palmer, M.R., Martí, J., and Sparks, R.S.J. (1998) Basanite–
606 Phonolite Lineages of the Teide–Pico Viejo Volcanic Complex, Tenerife, Canary
607 Islands. Journal of Petrology, 39(5), 905-936.
608 Ackerman, L., Ulrych, J., Řanda, Z., Erban, V., Hegner, E., Magna, T., Balogh, K., Frána, J.,
609 Lang, M., and Novák, J.K. (2015) Geochemical characteristics and petrogenesis of
610 phonolites and trachytic rocks from the České Středohoří Volcanic Complex, the
611 Ohře Rift, Bohemian Massif. Lithos, 224, 256-271.
612 Andújar, J., and Scaillet, B. (2012) Experimental Constraints on Parameters Controlling the
613 Difference in the Eruptive Dynamics of Phonolitic Magmas: the Case of Tenerife
614 (Canary Islands). Journal of Petrology, 53(9), 1777-1806.
615 Azzouni-Sekkal, A., Bonin, B., Benhallou, A., Yahiaoui, R., and Liégeois, J.-P. (2007)
616 Cenozoic alkaline volcanism of the Atakor massif, Hoggar, Algeria. Cenozoic
617 volcanism in the Mediterranean area, 418, 321.
618 Bachmann, O., and Bergantz, G.W. (2004) On the origin of crystal-poor rhyolites: extracted
619 from batholithic crystal mushes. Journal of Petrology, 45(8), 1565-1582.
620 Bachmann, O., and Huber, C. (2016) Silicic magma reservoirs in the Earth's crust. American
621 Mineralogist, 101(11), 2377-2404.

622 Bailey, D., and Schairer, J. (1964) Feldspar-liquid equilibria in peralkaline liquids; the
623 orthoclase effect. American Journal of Science, 262(10), 1198-1206.
624 Berndt, J., Holtz, F., and Koepke, J. (2001) Experimental constraints on storage conditions in
625 the chemically zoned phonolitic magma chamber of the Laacher See volcano.
626 Contributions to Mineralogy and Petrology, 140(4), 469-486.
627 Bohannon, R.G., Naeser, C.W., Schmidt, D.L., and Zimmermann, R.A. (1989) The timing of
628 uplift, volcanism, and rifting peripheral to the Red Sea: a case for passive rifting?
629 Journal of Geophysical Research: Solid Earth, 94(B2), 1683-1701.
630 Brenna, M., Cronin, S.J., Smith, I.E.M., Sohn, Y.K., and Maas, R. (2012) Spatio-temporal
631 evolution of a dispersed magmatic system and its implications for volcano growth,
632 Jeju Island Volcanic Field, Korea. Lithos, 148(0), 337-352.
633 Brenna, M., Nakada, S., Miura, D., Toshida, K., Ito, H., Hokanishi, N., and Nakai, S.i. (2015)
634 A trachyte–syenite core within a basaltic nest: filtering of primitive injections by a
635 multi-stage magma plumbing system (Oki-Dōzen, south-west Japan). Contributions to
636 Mineralogy and Petrology, 170(2), 1-21.
637 Brenna, M., Price, R., Cronin, S.J., Smith, I.E.M., Sohn, Y.K., Kim, G.B., and Maas, R.
638 (2014) Final magma storage depth modulation of explosivity and trachyte/phonolite
639 genesis at an intraplate volcano: a case study from Ulleung Island, Republic of Korea.
640 Journal of Petrology, 55(4), 709-747.
641 Brown, R., Civetta, L., Arienzo, I., D'Antonio, M., Moretti, R., Orsi, G., Tomlinson, E.,
642 Albert, P., and Menzies, M. (2014) Geochemical and isotopic insights into the
643 assembly, evolution and disruption of a magmatic plumbing system before and after a
644 cataclysmic caldera-collapse eruption at Ischia volcano (Italy). Contributions to
645 Mineralogy and Petrology, 168(3), 1035.

646 Camp, V.E., Hooper, P.R., Roobol, M.J., and White, D. (1987) The Madinah eruption, Saudi
647 Arabia: magma mixing and simultaneous extrusion of three basaltic chemical types.
648 Bulletin of Volcanology, 49(2), 489-508.
649 Camp, V.E., and Roobol, M.J. (1989) The Arabian continental alkali basalt province: Part I.
650 Evolution of Harrat Rahat, Kingdom of Saudi Arabia. Geological Society of America
651 Bulletin, 101(1), 71-95.
652 Carmichael, I.S.E., and MacKenzie, W. (1963) Feldspar-liquid equilibria in pantellerites; an
653 experimental study. American Journal of Science, 261(4), 382-396.
654 Caroff, M., Ambrics, C., Maury, R., and Cotten, J. (1997) From alkali basalt to phonolite in
655 hand-size samples: vapor-differentiation effects in the Bouzentes lava flow (Cantal,
656 France). Journal of Volcanology and Geothermal Research, 79(1), 47-61.
657 Caroff, M., Maury, R.C., Cotten, J., and Clément, J.-P. (2000) Segregation structures in
658 vapor-differentiated basaltic flows. Bulletin of Volcanology, 62(3), 171-187.
659 Cioni, R., Marianelli, P., and Santacroce, R. (1998) Thermal and compositional evolution of
660 the shallow magma chambers of Vesuvius: evidence from pyroxene phenocrysts and
661 melt inclusions. Journal of Geophysical Research: Solid Earth, 103(B8), 18277-
662 18294.
663 Coombs, D.S., Adams, C.J., Roser, B.P., and Reay, A. (2008) Geochronology and
664 geochemistry of the Dunedin Volcanic Group, eastern Otago, New Zealand. New
665 Zealand journal of geology and geophysics, 51(3), 195-218.
666 Coombs, D.S., and Wilkinson, J.F.G. (1969) Lineages and Fractionation Trends in
667 Undersaturated Volcanic Rocks from the East Otago Volcanic Province (New
668 Zealand) and Related Rocks. Journal of Petrology, 10(3), 440-501.

669 Davidson, J.P., and Wilson, I.R. (1989) Evolution of an alkali basalt—trachyte suite from
670 Jebel Marra volcano, Sudan, through assimilation and fractional crystallization. Earth
671 and Planetary Science Letters, 95(1-2), 141-160.
672 Deering, C., Cole, J., and Vogel, T. (2011) Extraction of crystal-poor rhyolite from a
673 hornblende-bearing intermediate mush: a case study of the caldera-forming Matahina
674 eruption, Okataina volcanic complex. Contributions to Mineralogy and Petrology,
675 161(1), 129-151.
676 Di Renzo, V., Wohletz, K., Civetta, L., Moretti, R., Orsi, G., and Gasparini, P. (2016) The
677 thermal regime of the Campi Flegrei magmatic system reconstructed through 3D
678 numerical simulations. Journal of Volcanology and Geothermal Research, 328, 210-
679 221.
680 Dufek, J., and Bachmann, O. (2010) Quantum magmatism: Magmatic compositional gaps
681 generated by melt-crystal dynamics. Geology, 38(8), 687-690.
682 Fabbrizio, A., and Carroll, M.R. (2008) Experimental constraints on the differentiation
683 process and pre-eruptive conditions in the magmatic system of Phlegraean Fields
684 (Naples, Italy). Journal of Volcanology and Geothermal Research, 171(1-2), 88-102.
685 Forni, F., Bachmann, O., Mollo, S., De Astis, G., Gelman, S.E., and Ellis, B.S. (2016) The
686 origin of a zoned ignimbrite: Insights into the Campanian Ignimbrite magma chamber
687 (Campi Flegrei, Italy). Earth and Planetary Science Letters, 449, 259-271.
688 Forni, F., Degruyter, W., Bachmann, O., De Astis, G., and Mollo, S. (2018) Long-term
689 magmatic evolution reveals the beginning of a new caldera cycle at Campi Flegrei.
690 Science Advances, 4(11), eaat9401.
691 Freda, C., Baker, D., and Ottolini, L. (2001) Reduction of water loss from gold-palladium
692 capsules during piston-cylinder experiments by use of pyrophyllite powder. American
693 Mineralogist, 86(3), 234-237.

694 Freda, C., Gaeta, M., Misiti, V., Mollo, S., Dolfi, D., and Scarlato, P. (2008) Magma–
695 carbonate interaction: an experimental study on ultrapotassic rocks from Alban Hills
696 (Central Italy). Lithos, 101(3-4), 397-415.
697 Freise, M., Holtz, F., Koepke, J., Scoates, J., and Leyrit, H. (2003) Experimental constraints
698 on the storage conditions of phonolites from the Kerguelen Archipelago.
699 Contributions to Mineralogy and Petrology, 145(6), 659-672.
700 Ghiorso, M.S., and Gualda, G.A. (2015) An H 2 O–CO 2 mixed fluid saturation model
701 compatible with rhyolite-MELTS. Contributions to Mineralogy and Petrology,
702 169(6), 53.
703 Ginibre, C., Wörner, G., and Kronz, A. (2004) Structure and dynamics of the Laacher See
704 magma chamber (Eifel, Germany) from major and trace element zoning in sanidine: a
705 cathodoluminescence and electron microprobe study. Journal of Petrology, 45(11),
706 2197-2223.
707 Grant, T.B., Milke, R., Pandey, S., and Jahnke, H. (2013) The Heldburg Phonolite, Central
708 Germany: Reactions between phonolite and xenocrysts from the upper mantle and
709 lower crust. Lithos, 182, 86-101.
710 Gualda, G.A., Ghiorso, M.S., Lemons, R.V., and Carley, T.L. (2012) Rhyolite-MELTS: a
711 modified calibration of MELTS optimized for silica-rich, fluid-bearing magmatic
712 systems. Journal of Petrology, 53(5), 875-890.
713 Harms, E., Gardner, J.E., and Schmincke, H.U. (2004) Phase equilibria of the Lower Laacher
714 See Tephra (East Eifel, Germany): constraints on pre-eruptive storage conditions of a
715 phonolitic magma reservoir. Journal of Volcanology and Geothermal Research,
716 134(1–2), 125-138.
717 Hay, D.E., and Wendlandt, R.F. (1995) The origin of Kenya rift plateau-type flood
718 phonolites: Results of high-pressure/high-temperature experiments in the systems

719 phonolite-H2O and phonolite-H2O-CO2. Journal of Geophysical Research: Solid
720 Earth, 100(B1), 401-410.
721 Hildreth, W., and Wilson, C.J. (2007) Compositional zoning of the Bishop Tuff. Journal of
722 Petrology, 48(5), 951-999.
723 Huber, C., Bachmann, O., and Manga, M. (2009) Homogenization processes in silicic magma
724 chambers by stirring and mushification (latent heat buffering). Earth and Planetary
725 Science Letters, 283(1-4), 38-47.
726 Iezzi, G., Mollo, S., Shahini, E., Cavallo, A., and Scarlato, P. (2014) The cooling kinetics of
727 plagioclase feldspar as revealed by electron-microprobe mapping. American
728 Mineralogist, 99(5-6), 898-907.
729 Irving, A.J., and Price, R.C. (1981) Geochemistry and evolution of Iherzolite-bearing
730 phonolitic lavas from Nigeria, Australia, East Germany and New Zealand.
731 Geochimica et Cosmochimica Acta, 45(8), 1309-1320.
732 Kano, K., Matsuura, H., and Yamauchi, S. (1997) Miocene rhyolitic welded tuff infilling a
733 funnel-shaped eruption conduit Shiotani, southeast of Matsue, SW Japan. Bulletin of
734 Volcanology, 59(2), 125-135.
735 Katz, R.F., Spiegelman, M., and Holtzman, B. (2006) The dynamics of melt and shear
736 localization in partially molten aggregates. Nature, 442(7103), 676.
737 Kim, J., Park, J.-W., Lee, M.J., Lee, J.I., and Kyle, P.R. (2018) Evolution of alkalic magma
738 systems: insight from coeval evolution of sodic and potassic fractionation lineages at
739 the Pleiades volcanic complex, Antarctica. Journal of Petrology, 60(1), 117-150.
740 Kyle, P., Moore, J., and Thirlwall, M. (1992) Petrologic evolution of anorthoclase phonolite
741 lavas at Mount Erebus, Ross Island, Antarctica. Journal of Petrology, 33(4), 849-875.

742 Laporte, D., Lambart, S., Schiano, P., and Ottolini, L. (2014) Experimental derivation of
743 nepheline syenite and phonolite liquids by partial melting of upper mantle peridotites.
744 Earth and Planetary Science Letters, 404, 319-331.
745 Le Maitre, R.W. (2002) Igneous Rocks: A Classification and Glossary of Terms. 240 p.
746 Cambridge University Press.
747 Legendre, C., Maury, R.C., Caroff, M., Guillou, H., Cotten, J., Chauvel, C., Bollinger, C.,
748 Hémond, C., Guille, G., Blais, S., Rossi, P., and Savanier, D. (2005) Origin of
749 Exceptionally Abundant Phonolites on Ua Pou Island (Marquesas, French Polynesia):
750 Partial Melting of Basanites Followed by Crustal Contamination. Journal of
751 Petrology, 46(9), 1925-1962.
752 LeMasurier, W., Choi, S., Kawachi, Y., Mukasa, S., and Rogers, N.W. (2011) Evolution of
753 pantellerite-trachyte-phonolite volcanoes by fractional crystallization of basanite
754 magma in a continental rift setting, Marie Byrd Land, Antarctica. Contributions to
755 Mineralogy and Petrology, 162(6), 1175-1199.
756 Macdonald, R., Bagiński, B., Leat, P.T., White, J.C., and Dzierżanowski, P. (2011) Mineral
757 stability in peralkaline silicic rocks: information from trachytes of the Menengai
758 volcano, Kenya. Lithos, 125(1-2), 553-568.
759 Martel, C., Champallier, R., Prouteau, G., Pichavant, M., Arbaret, L., Balcone-Boissard, H.,
760 Boudon, G., Boivin, P., Bourdier, J.-L., and Scaillet, B. (2013) Trachyte phase
761 relations and implication for magma storage conditions in the Chaîne des Puys
762 (French Massif Central). Journal of Petrology, 54(6), 1071-1107.
763 Masotta, M., Freda, C., and Gaeta, M. (2012) Origin of crystal-poor, differentiated magmas:
764 insights from thermal gradient experiments. Contributions to Mineralogy and
765 Petrology, 163(1), 49-65.

766 Masotta, M., Gaeta, M., Gozzi, F., Marra, F., Palladino, D., and Sottili, G. (2010) H 2 O-and
767 temperature-zoning in magma chambers: the example of the Tufo Giallo della Via
768 Tiberina eruptions (Sabatini Volcanic District, central Italy). Lithos, 118(1), 119-130.
769 Masotta, M., Mollo, S., Freda, C., Gaeta, M., and Moore, G. (2013) Clinopyroxene–liquid
770 thermometers and barometers specific to alkaline differentiated magmas.
771 Contributions to Mineralogy and Petrology, 166(6), 1545-1561.
772 Masotta, M., Mollo, S., Gaeta, M., and Freda, C. (2016) Melt extraction in mush zones: The
773 case of crystal-rich enclaves at the Sabatini Volcanic District (central Italy). Lithos,
774 248, 288-292.
775 McLean, D., Albert, P.G., Nakagawa, T., Suzuki, T., Staff, R.A., Yamada, K., Kitaba, I.,
776 Haraguchi, T., Kitagawa, J., and Members, S.P. (2018) Integrating the Holocene
777 tephrostratigraphy for East Asia using a high-resolution cryptotephra study from Lake
778 Suigetsu (SG14 core), central Japan. Quaternary Science Reviews, 183, 36-58.
779 Moufti, M., Moghazi, A., and Ali, K. (2013) 40 Ar/39 Ar geochronology of the Neogene-
780 Quaternary Harrat Al-Madinah intercontinental volcanic field, Saudi Arabia:
781 implications for duration and migration of volcanic activity. Journal of Asian Earth
782 Sciences, 62, 253-268.
783 Moufti, M.R., Moghazi, A.M., and Ali, K.A. (2012) Geochemistry and Sr–Nd–Pb isotopic
784 composition of the Harrat Al-Madinah Volcanic Field, Saudi Arabia. Gondwana
785 Research, 21(2–3), 670-689.
786 Moufti, M.R., and Németh, K. (2016) Geoheritage of Volcanic Harrats in Saudi Arabia.
787 Springer.
788 Murcia, H., Németh, K., Moufti, M.R., Lindsay, J.M., El-Masry, N., Cronin, S.J., Qaddah,
789 A., and Smith, I.E.M. (2014) Late Holocene lava flow morphotypes of northern

790 Harrat Rahat, Kingdom of Saudi Arabia: Implications for the description of
791 continental lava fields. Journal of Asian Earth Sciences, 84(0), 131-145.
792 Norrish, K., and Hutton, J.T. (1969) An accurate X-ray spectrographic method for the
793 analysis of a wide range of geological samples. Geochimica et Cosmochimica Acta,
794 33(4), 431-453.
795 Panter, K.S., Kyle, P.R., and Smellie, J.L. (1997) Petrogenesis of a Phonolite–Trachyte
796 Succession at Mount Sidley, Marie Byrd Land, Antarctica. Journal of Petrology,
797 38(9), 1225-1253.
798 Petrelli, M., Poli, G., Perugini, D., and Peccerillo, A. (2005) PetroGraph: A new software to
799 visualize, model, and present geochemical data in igneous petrology. Geochemistry,
800 Geophysics, Geosystems (G^3), 6, Q07011.
801 Ridolfi, F., Renzulli, A., Macdonald, R., and Upton, B.G.J. (2006) Peralkaline syenite
802 autoliths from Kilombe volcano, Kenya Rift Valley: Evidence for subvolcanic
803 interaction with carbonatitic fluids. Lithos, 91(1–4), 373-392.
804 Riishuus, M.S., Peate, D.W., Tegner, C., Wilson, J.R., and Brooks, C.K. (2008) Petrogenesis
805 of cogenetic silica-oversaturated and-undersaturated syenites by periodic recharge in a
806 crustally contaminated magma chamber: the Kangerlussuaq intrusion, East
807 Greenland. Journal of Petrology, 49(3), 493-522.
808 Romano, P., Andújar, J., Scaillet, B., Romengo, N., Di Carlo, I., and Rotolo, S.G. (2018)
809 Phase equilibria of Pantelleria trachytes (Italy): constraints on pre-eruptive conditions
810 and on the metaluminous to peralkaline transition in silicic magmas. Journal of
811 Petrology.
812 Runge, M.G., Bebbington, M.S., Cronin, S.J., Lindsay, J.M., Kenedi, C.L., and Moufti,
813 M.R.H. (2014) Vents to events: determining an eruption event record from volcanic

814 vent structures for the Harrat Rahat, Saudi Arabia. Bulletin of Volcanology, 76(3), 1-
815 16.
816 Shea, T., Gurioli, L., Houghton, B.F., Cioni, R., and Cashman, K.V. (2011) Column collapse
817 and generation of pyroclastic density currents during the AD 79 eruption of Vesuvius:
818 the role of pyroclast density. Geology, 39(7), 695-698.
819 Stelten, M.E., Downs, D.T., Dietterich, H.R., Mahood, G.A., Calvert, A.T., Sisson, T.W.,
820 Zahran, H., and Shawali, J. (2018) Timescales of magmatic differentiation from alkali
821 basalt to trachyte within the Harrat Rahat volcanic field, Kingdom of Saudi Arabia.
822 Contributions to Mineralogy and Petrology, 173(8), 68.
823 Stormer, J.C.J., and Nicholls, J. (1978) XLFRAC: a program for the interactive testing of
824 magmatic differentiation models. Computers & Geosciences, 4, 143-159.
825 Thompson, G., Smith, I., and Malpas, J. (2001) Origin of oceanic phonolites by crystal
826 fractionation and the problem of the Daly gap: an example from Rarotonga.
827 Contributions to Mineralogy and Petrology, 142(3), 336-346.
828 Thompson, R.N., and MacKenzie, W. (1967) Feldspar-liquid equilibria in peralkaline acid
829 liquids; an experimental study. American Journal of Science, 265(8), 714-734.
830 Upton, B. (1974) The alkaline province of south-west Greenland, p. 221-238. John Wiley &
831 Sons, Chichester, UK.
832 Valentine, G., and Gregg, T. (2008) Continental basaltic volcanoes—processes and problems.
833 Journal of Volcanology and Geothermal Research, 177(4), 857-873.
834 White, J.C., Espejel-García, V.V., Anthony, E.Y., and Omenda, P. (2012) Open System
835 evolution of peralkaline trachyte and phonolite from the Suswa volcano, Kenya rift.
836 Lithos, 152(0), 84-104.
837 Wiesmaier, S., Deegan, F.M., Troll, V.R., Carracedo, J.C., Chadwick, J.P., and Chew, D.M.
838 (2011) Magma mixing in the 1100 AD Montaña Reventada composite lava flow,

Tenerife, Canary Islands: interaction between rift zone and central volcano plumbing systems. Contributions to Mineralogy and Petrology, 162(3), 651-669.

Wörner, G., and Schmincke, H.-U. (1984) Petrogenesis of the Zoned Laacher See Tephra. Journal of Petrology, 25(4), 836-851.

Figure captions

Figure 1. a) Location of Cenozoic intraplate volcanic area in the Arabian Plate. b) The Harrat Rahat Volcanic Field (outline dashed) encroaches the southern suburbs of Al-Madinah city (shaded). The principal evolved eruptive centres occur in the central portion of the field. c) The Al Shaatha pyroclastic deposit are light brown, and the pre-eruptive basaltic basement is dark grey/black. Location of the sampled sections (SH01 to SH05) of the Al Shaatha eruption along a wadi on the western side of the volcano. The crater rim (dashed) is a very subdued geomorphic feature. Base images for a), b) and c) are from Google Earth, Landsat, Copernicus, DigitalGlobe.

Figure 2. a) Total alkali vs. silica (TAS) diagram (Le Maitre, 2002) showing whole rock compositions of the Al Shaatha eruptive sequence. The pink area indicates the overall products from the Harrat Rahat Volcanic Field (Moufti et al., 2012). SMA and SMB refer to starting materials for Experimental Sets A and B respectively. b-j) stratigraphically ordered chemical variability in the Al Shaatha eruption from samples collected at localities SH05 and SH01 (top).

Figure 3. Representative photomicrographs (PPL) of selected Al Shaatha eruption products (lapilli and bombs). a) benmoreite with fayalitic olivine (Ol), clinopyroxene (Cpx), feldspar

(Feld) and titanomagnetite (Ti-Mag) microphenocrysts in a vesiculated (ves) groundmass of Feld + Cpx + Ti-Mag. b) trachyte, with overall similar mineralogy. Note the orange iddingsitisation of the olivine. Feldspar microphenocrysts and groundmass crystals show good alignment. c) and d) phonolite exhibiting identical mineral assemblage of trachyte in b) but have diktytaxitic texture and contain sieve-textured anothoclase glomerocrysts (d). e) Backscatter Electron (BSE) image of the benmoreite. Note the high degree of vesicularity and lack of major zonation in the clinopyroxene. f) BSE image of feldspar (anorthoclase) glomerocryst in the phonolite. Note the lack of zonation in the individual crystals.

Figure 4. Compositions of natural and experimental clinopyroxene crystals.

Figure 5. Composition of natural and experimental feldspars.

Figure 6. BSE (backscattered electron) images of selected experimental products. a), b) and c) are from Experimental Set A, and d), e), and f) are from Experimental Set B.

Figure 7. a) Relationship between degree of crystallization and experimental temperature and added H_2O in 200 and 500 MPa experiments. Experiments with CO_2 only are considered anhydrous. b) Variation of feldspar/clinopyroxene modal ratio with experimental temperature and added H_2O in 200 MPa experiments.

*Figure 8. Experimental glass compositions obtained by using the benmoreite (**A**) as starting composition. Star symbols represent the whole rock composition of natural samples. **A** and **B** indicate the starting materials for the two experimental sets.*

*Figure 9. Experimental glass compositions obtained by using the trachyte (**B**) as starting material. Star symbols represent the whole rock composition of natural samples. **A** and **B** indicate the starting materials for the two experimental sets.*

Figure 10. Evolution of peralkalinity and sodicity (Thompson and MacKenzie, 1967) of the experimental glasses and natural whole rock samples from Al Shaatha. Symbols as in Figures 8 and 9.

Figure 11. Schematic illustration (not to scale) of the proposed scenario for the formation of phonolite erupted at Al Shaatha. An initial stalled intrusion crystallizes extensively to form a anorthoclase-dominated crystal mush with interstitial phonolitic melt. A subsequent injection from the deeper plumbing remobilizes and interacts with the crystal mush, resorbs some anorthoclase and entrains the interstitial melt.

Table captions

Table 1. Whole rock major element abundances of tephras erupted at Al Shaatha. Sample SH1A is the starting material for Experimental Set A and sample SH5C is starting material for Experimental Set B. SD EPMA is the standard deviation of microprobe analyses (n = 10) of the starting glass for the two experiments (SMA and SMB).

Table 2. Experimental conditions

Table 3. Least squares crystal fractionation modeling of Al Shaatha products.

Table 1. Whole-rock major element abundances of tephras erupted at Al Shaatha. Sample SH1A is the starting material for Experimental Set A and sample SH5C is starting material for Experimental Set B. SD EPMA is the standard deviation of microprobe analyses (n = 10) of the starting glass for the two experiments (SMA and SMB).

	SH1A (A)	SMA SD EPMA	SH2B	SH4A	SH4B	SH4C	SH5B
SiO_2	58.83	1.24	60.22	60.77	60.44	59.40	61.61
TiO_2	0.60	0.10	0.47	0.36	0.40	0.57	0.28
Al_2O_3	16.65	0.54	16.96	17.30	17.02	16.87	17.61
FeO_{tot}	8.32	0.48	7.64	7.18	7.47	8.31	6.39
MnO	0.26	0.06	0.25	0.24	0.25	0.26	0.22
MgO	0.60	0.74	0.48	0.37	0.30	0.57	0.33
CaO	4.03	0.13	2.95	2.41	2.46	2.89	1.84
Na_2O	6.49	0.17	6.64	6.43	6.90	6.90	6.41
K_2O	3.94	0.17	4.18	4.80	4.60	3.95	5.20
P_2O_5	0.30	0.03	0.21	0.14	0.16	0.28	0.10
$Tot_{anhydrous}$	100.00		100.00	100.00	100.00	100.00	100.00
H_2O	0.63		0.43	0.62	0.09	0.03	0.58
LOI	0.87		0.65	0.86	0.47	0.09	1.18

	SH5C (B)	SMB SD EPMA	SH5D	SH5E	SH5F	SH5I	SH5J
SiO_2	61.88	0.92	60.90	59.97	60.78	59.93	59.27
TiO_2	0.26	0.03	0.26	0.28	0.33	0.44	0.59
Al_2O_3	17.51	0.22	17.15	16.99	17.21	17.09	17.07
FeO_{tot}	6.32	0.17	6.19	6.24	6.86	7.93	8.48
MnO	0.22	0.04	0.22	0.22	0.24	0.26	0.27
MgO	0.21	0.03	0.19	0.13	0.28	0.45	0.55
CaO	1.60	0.06	1.69	1.80	2.71	2.50	2.93
Na_2O	6.65	0.14	8.29	9.43	6.57	6.79	6.55
K_2O	5.26	0.05	5.03	4.84	4.89	4.40	4.00
P_2O_5	0.10	0.04	0.10	0.10	0.14	0.21	0.30
$Tot_{anhydrous}$	100.00		100.00	100.00	100.00	100.00	100.00
H_2O	0.60		1.26	0.47	0.47	0.30	0.42
LOI	0.58		1.25	0.98	1.13	0.38	0.48

Table 2. Experimental conditions

Experiment	T (°C)	P (MPa)	H_2O added (wt.%)	CO_2 added (wt.%)	Duration (h)	Phase assemblage and modal proportions (%)
Experiments with benmoreite (A) starting composition						
A14	1,150	500	0.0	0.0	24	Gl (98) + Cpx (<1) + Ti-Mag (1)
A23	1,050	500	0.0	0.0	70	Gl (60) + Feld (34) + Cpx (3) + Ti-Mag (3)
A26	1,050	500	0.0	0.27	70	Gl (63) + Feld (29) + Cpx (5) + Ti-Mag (3)
A10	1,000	200	4.0	0.0	24	Gl (98) + Cpx (<1) + Ti-Mag (2)
A3	1,000	200	0.0	0.0	24	Gl (22) + Feld (71) + Cpx (4) + Ti-Mag (3)
A4	900	200	0.0	0.0	70	Gl (25) + Feld (65) + Cpx (7) + Ti-Mag (3)
A5	900	200	0.0	0.0	24	Gl (35) + Feld (58) + Cpx (5) + Ti-Mag (2)
A15	900	200	4.0	0.0	24	Gl (53) + Feld (40) + Cpx (3) + Ti-Mag (3)
A25	850	500	10.1	0.0	12	Gl (92) + Cpx (4) + Ti-Mag (4)
A22	850	500	0.0	0.25	12	Gl (37) + Feld (55) + Cpx (5) + Ti-Mag (3)
A20	850	200	0.0	0.5	25	Gl (2) + Feld (86) + Cpx (8) + Ti-Mag (3)
A21	850	200	7.7	0.0	25	Gl (<1) + Feld (88) + Cpx (10) + Ti-Mag (2)
Experiments with trachyte (B) starting composition						
B10	1,000	500	0.0	0.0	44	Gl (66) + Feld (32) + Cpx (<1) + Ti-Mag (2)
B11	1,000	500	0.0	0.0	44	Gl (69) + Feld (28) + Cpx (1) + Ti-Mag (2)
B5	1,000	200	0.0	0.0	50	Gl (38) + Feld (60) + Cpx (1) + Ti-Mag (2)
B6	1,000	200	0.0	0.31	50	Gl (48) + Feld (49) + Cpx (<1) + Ti-Mag (2)
B12	950	500	7.1	0.0	44	Gl (100)
B13	950	500	0.0	0.0	44	Gl (97) + Ti-Mag (3)
B1	950	500	0.0	0.0	24	Gl (98) + Ti-Mag (2)
B1b	950	200	5.1	0.0	24	Gl (97) + Ti-Mag (3)
B2	950	200	0.0	0.0	24	Gl (27) + Feld (70) + Cpx (1) + Ti-Mag (2)
B9	900	500	5.1	0.0	48	Gl (99) + Ti-Mag (1)
B3	900	200	5.1	0.0	24	Gl (67) + Feld (30) + Cpx (1) + Ti-Mag (2)
B4	900	200	0.0	0.0	24	Gl (7) + Feld (90) + Cpx (2) + Ti-Mag (1)
B8	850	200	0.0	0.0	70	Gl (4) + Feld (92) + Cpx (2) + Ti-Mag (2)
B7	850	200	4.6	0.0	70	Gl (12) + Feld (84) + Cpx (2) + Ti-Mag (2)

Table 3. Least squares crystal fractionation modeling of Al Shaatha products.

	Initial melt *SH5C*	Final melt *SH5E*	Feldspar *SH5E_ feldpsar glomero 14*	Pyroxene *SH5E_ mafic 2*	Oxide *SH5C_oxid e gdm 3*	Observed differenc e	Calculated difference	Obs-Calc residuals
SiO_2	61.88	59.97	65.99	48.56	0.95	-1.90	-1.56	-0.35
TiO_2	0.26	0.28	0.05	0.35	1.11	0.02	0.13	-0.12
Al_2O_3	17.51	16.99	19.85	1.79	0.60	-0.52	-0.72	0.20
FeO_{tot}	6.32	6.24	0.21	24.19	95.92	-0.07	0.09	-0.17
MnO	0.22	0.22	0.00	1.02	0.64	0.00	0.10	-0.11
MgO	0.21	0.13	0.01	2.87	0.16	-0.08	-0.04	-0.04
CaO	1.60	1.80	0.74	20.1	0.04	0.20	-0.03	0.23
Na_2O	6.65	9.43	6.57	1.10	0.47	2.79	2.79	0.00
K_2O	5.26	4.84	6.56	0.01	0.11	-0.43	-0.84	0.41
P_2O_5	0.10	0.10	0.01	0.00	0.00	0.00	0.07	-0.07
Total	100.00	100.00	100.00	100.00	100.00			
							SSR =	0.44
Fractionated amount			71.97	4.69	3.80			
% of removed			89.45	5.83	4.72			

Figure 1

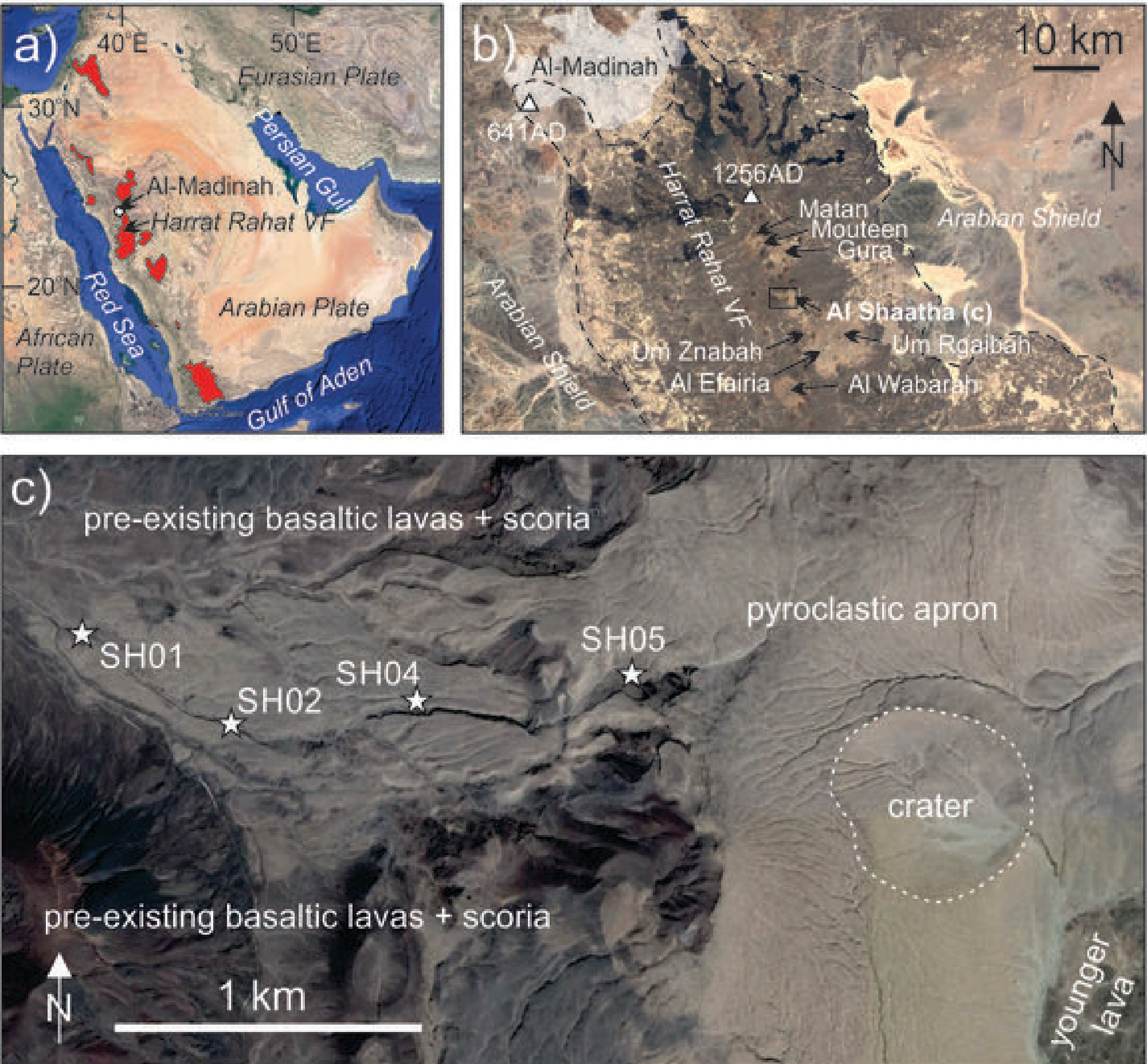
a)
40°E
50°E
Eurasian Plate
30°N
Persian Gulf
Al-Madinah
Harrat Rahat VF
20°N
Red Sea
Arabian Plate
African Plate
Gulf of Aden
b)
10 km
Al-Madinah
641AD
1256AD
Harrat Rahat VF
Matan
Mouteen
Gura
Arabian Shield
N
Arabian Shield
Al Shaatha (c)
Um Rgaibah
Um Znabah
Al Efairia
Al Wabarah
c)
pre-existing basaltic lavas + scoria
pyroclastic apron
SH01
SH02
SH04
SH05
crater
pre-existing basaltic lavas + scoria
younger lava
N
1 km

Figure 2

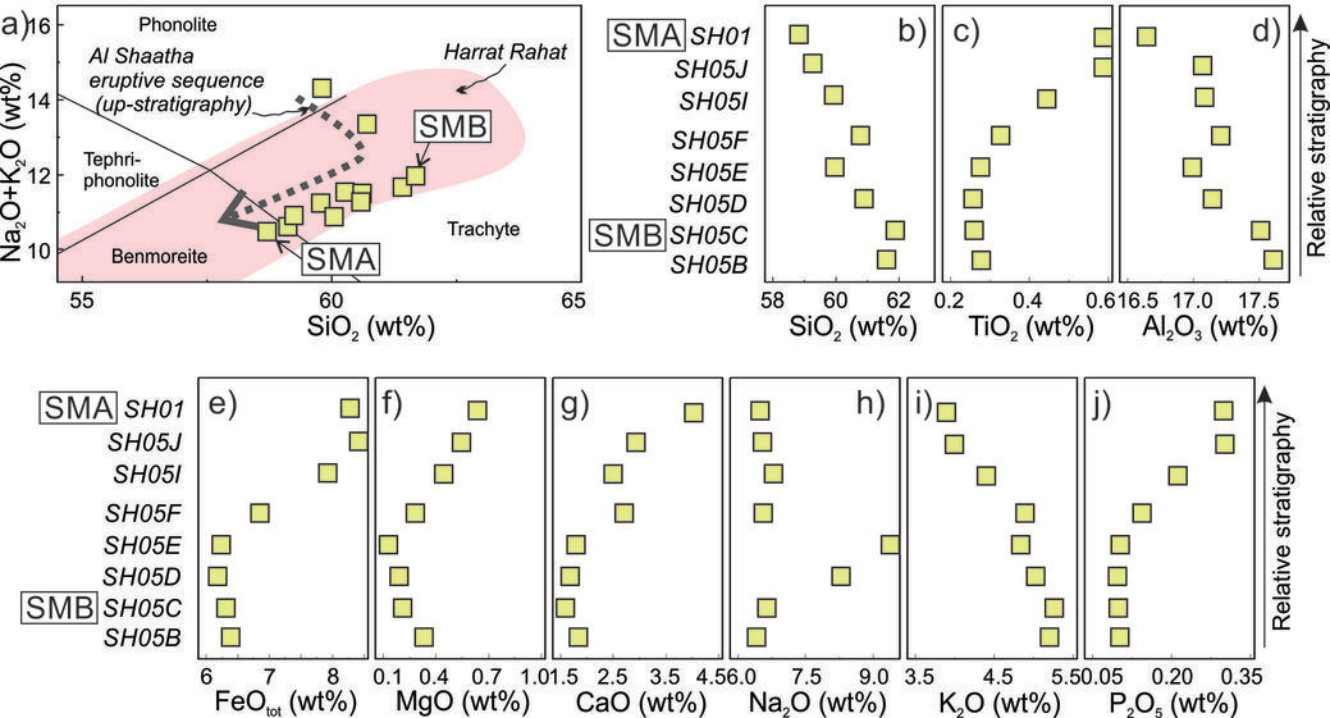
a)
Phonolite
Al Shaatha
eruptive sequence
(up-stratigraphy)
Harrat Rahat
SMB
Tephri-
phonolite
Trachyte
Benmoreite
SMA
Na2O+K2O (wt%)
SiO2 (wt%)
SMA SH01
SH05J
SH05I
SH05F
SH05E
SH05D
SMB SH05C
SH05B
b)
c)
d)
SiO2 (wt%)
TiO2 (wt%)
Al2O3 (wt%)
Relative stratigraphy
e)
f)
g)
h)
i)
j)
FeOtot (wt%)
MgO (wt%)
CaO (wt%)
Na2O (wt%)
K2O (wt%)
P2O5 (wt%)

Figure 3

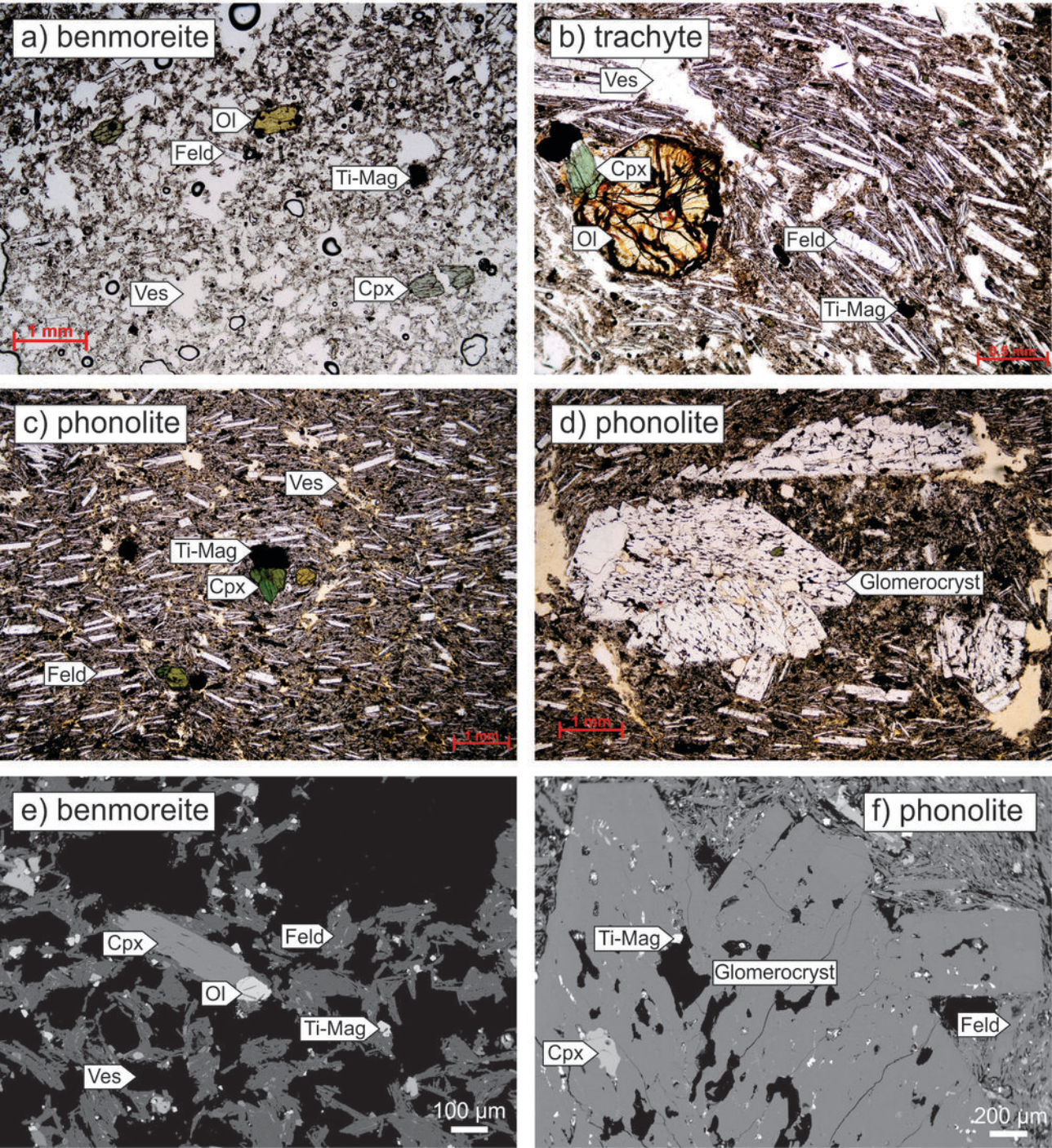
a) benmoreite
Ol
Feld
Ti-Mag
Ves
Cpx
1 mm
b) trachyte
Ves
Cpx
Ol
Feld
Ti-Mag
0.5 mm
c) phonolite
Ves
Ti-Mag
Cpx
Feld
1 mm
d) phonolite
Glomerocryst
1 mm
e) benmoreite
Cpx
Feld
Ol
Ti-Mag
Ves
100 µm
f) phonolite
Ti-Mag
Glomerocryst
Feld
Cpx
200 µm

Figure 4

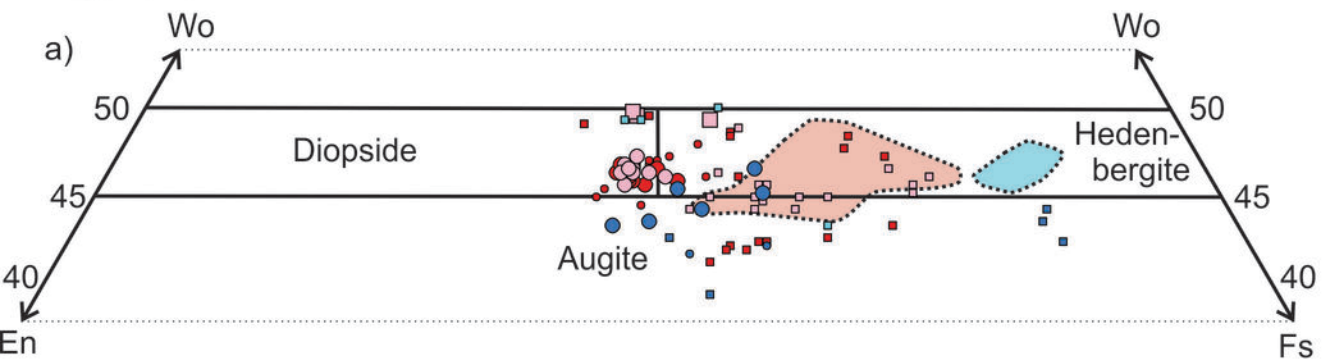

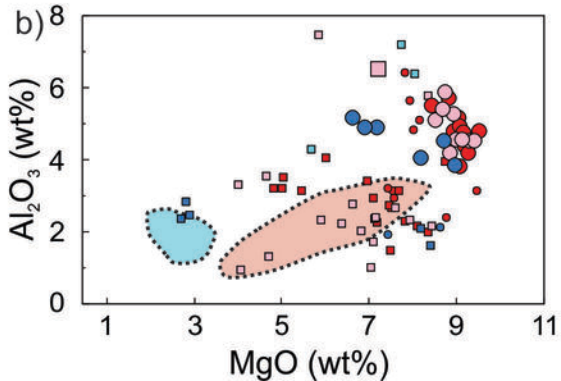

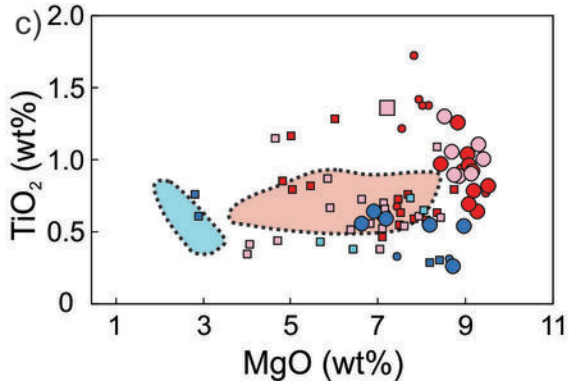

	A (benmoreite)		B (trachyte)	
Natural samples				
A starting material	dry		+ H_2O or CO_2	
Pressure (MPa)	500	200	500	200
≤950 °C		■	□	▫
≥1000 °C	●	•	○	
B starting material	dry		+ H_2O or CO_2	
Pressure (MPa)	500	200	500	200
≤950 °C		■		▫
≥1000 °C	●	•		

Figure 5

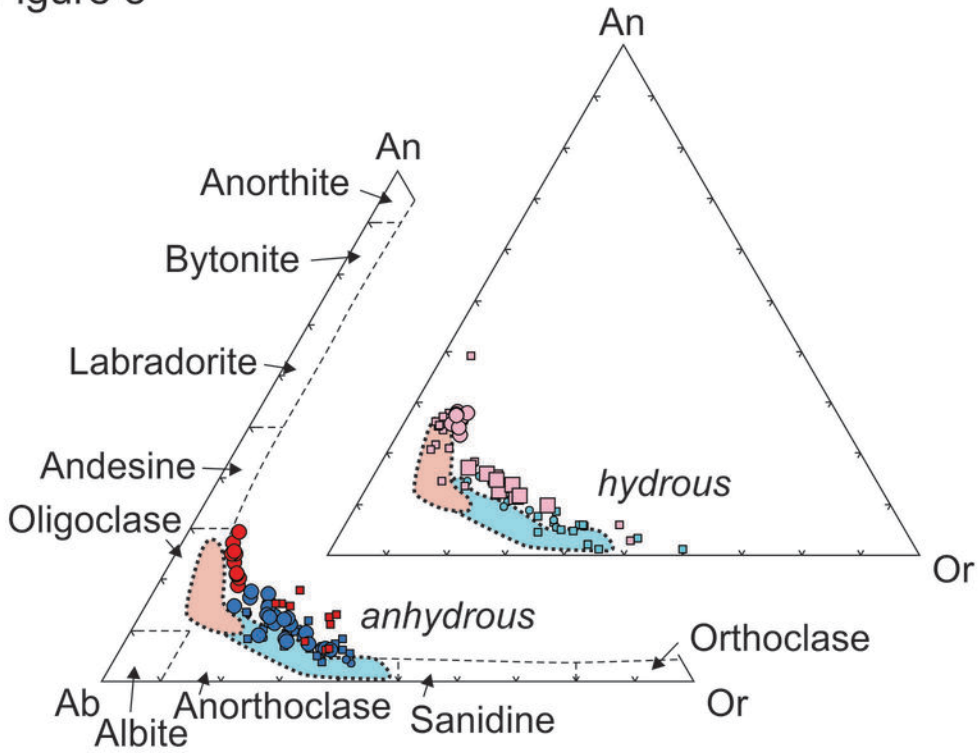

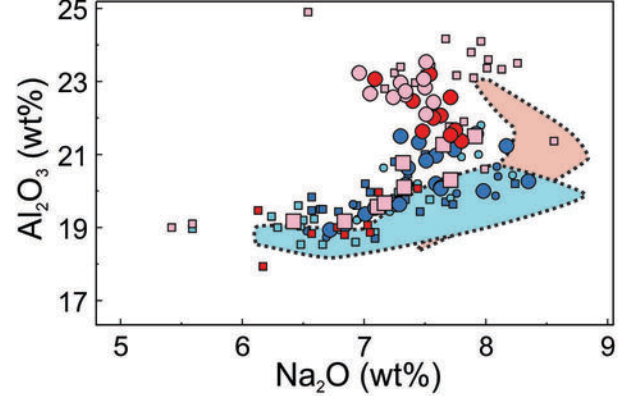

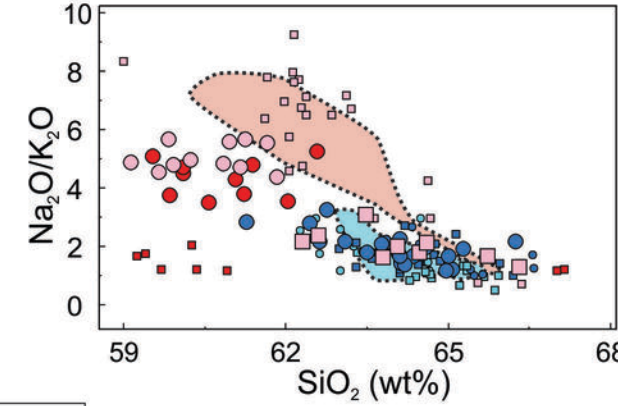

	A (benmoreite)	B (trachyte)
Natural samples		

A starting material	dry		+ H_2O or CO_2	
Pressure (MPa)	500	200	500	200
≤950 °C				
≥1000 °C				

B starting material	dry		+ H_2O or CO_2	
Pressure (MPa)	500	200	500	200
≤950 °C				
≥1000 °C				

Figure 6

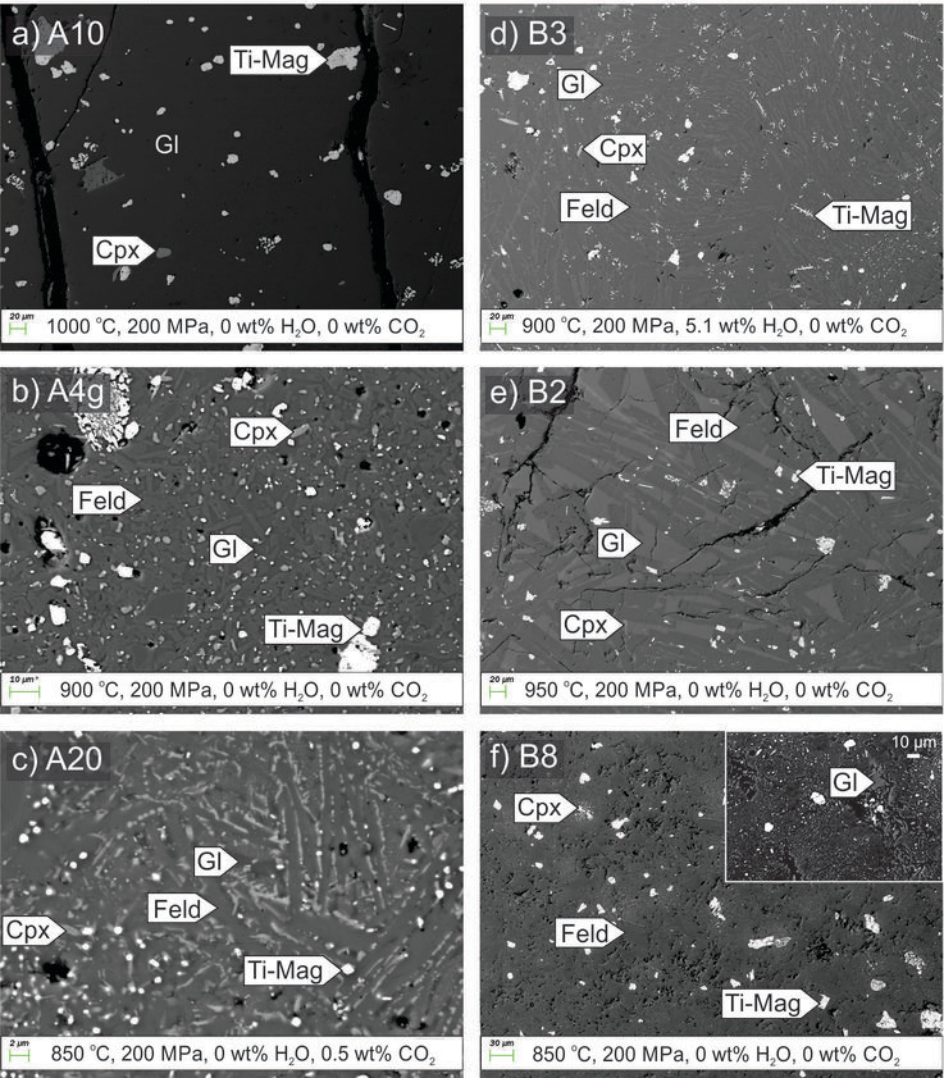
Experiment set A
Experiment set B
a) A10
Ti-Mag
Gl
Cpx
20 µm
1000 °C, 200 MPa, 0 wt% H2O, 0 wt% CO2
d) B3
Gl
Cpx
Feld
Ti-Mag
20 µm
900 °C, 200 MPa, 5.1 wt% H2O, 0 wt% CO2
b) A4g
Cpx
Feld
Gl
Ti-Mag
10 µm
900 °C, 200 MPa, 0 wt% H2O, 0 wt% CO2
e) B2
Feld
Ti-Mag
Gl
Cpx
20 µm
950 °C, 200 MPa, 0 wt% H2O, 0 wt% CO2
c) A20
Gl
Feld
Cpx
Ti-Mag
2 µm
850 °C, 200 MPa, 0 wt% H2O, 0.5 wt% CO2
f) B8
10 µm
Gl
Cpx
Feld
Ti-Mag
30 µm
850 °C, 200 MPa, 0 wt% H2O, 0 wt% CO2

Figure 7

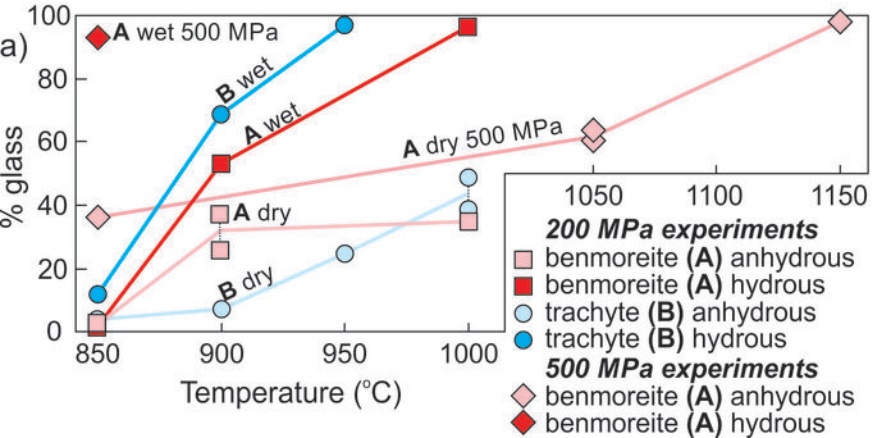
a)
% glass
Temperature (°C)
A wet 500 MPa
B wet
A wet
A dry 500 MPa
A dry
B dry
200 MPa experiments
benmoreite (A) anhydrous
benmoreite (A) hydrous
trachyte (B) anhydrous
trachyte (B) hydrous
500 MPa experiments
benmoreite (A) anhydrous
benmoreite (A) hydrous

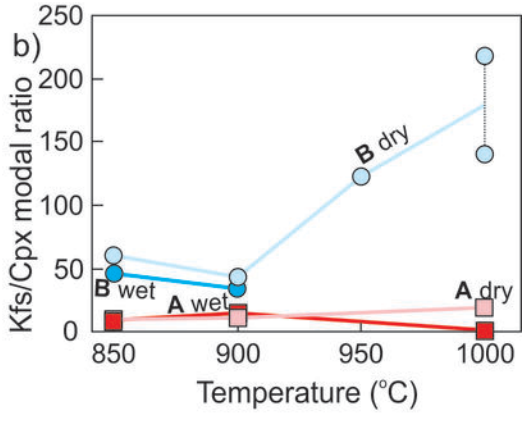
b)
Kfs/Cpx modal ratio
Temperature (°C)
B dry
B wet
A wet
A dry

Figure 8

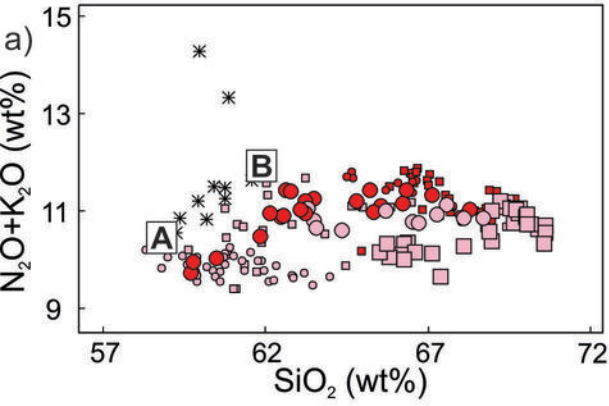

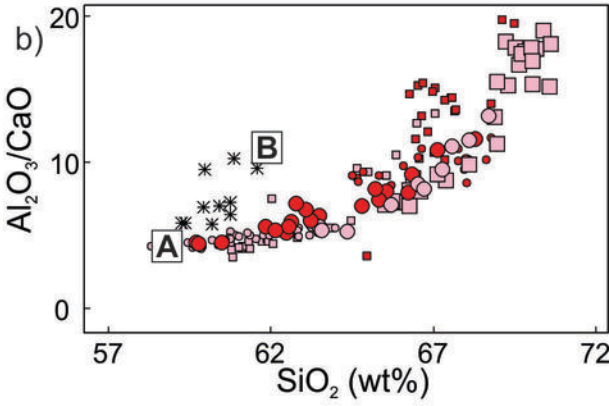

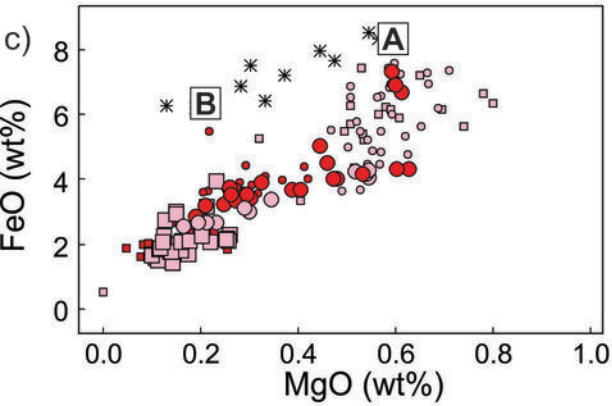

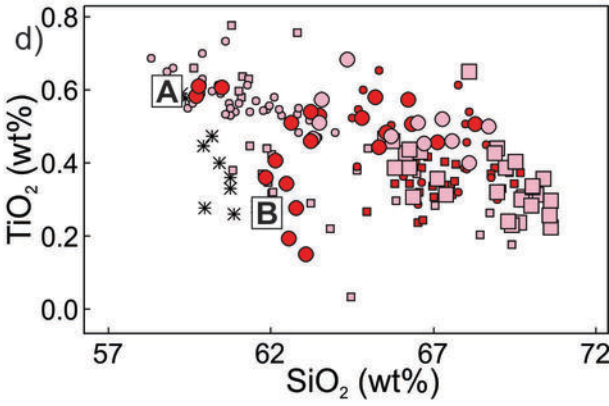

A starting material	dry		+ H_2O or CO_2	
Pressure (MPa)	500	200	500	200
≤950 °C		■	□	□
≥1000 °C	●	•	○	◦

Figure 9

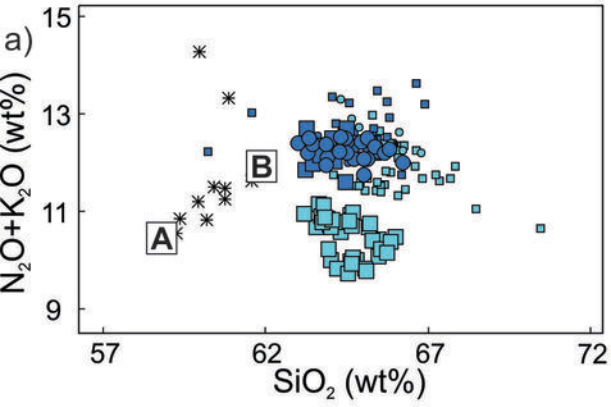

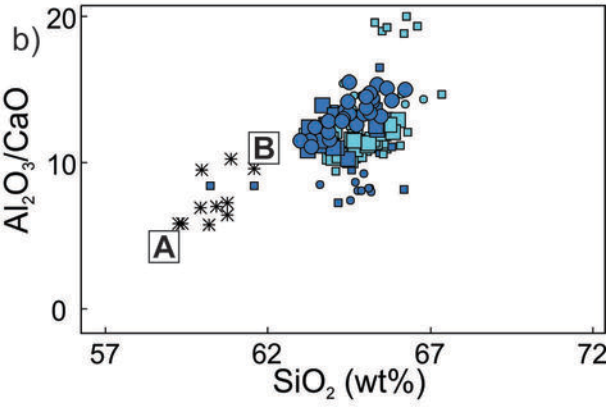

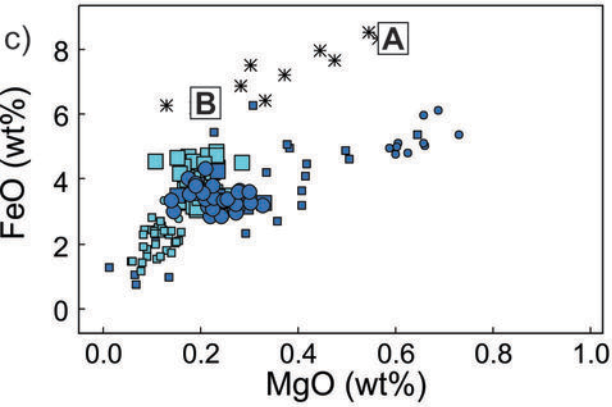

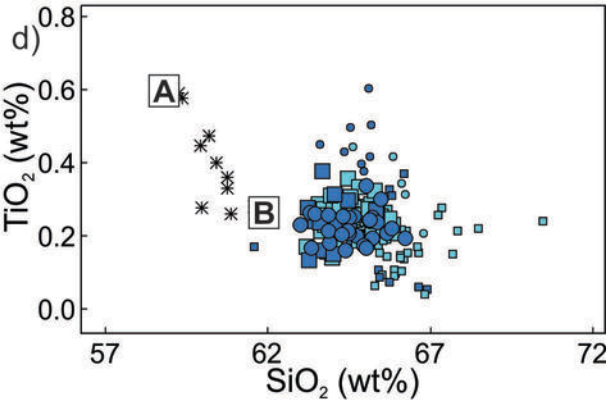

B starting material	dry		+ H_2O or CO_2	
Pressure (MPa)	500	200	500	200
≤950 °C	■	▪	□	▫
≥1000 °C	●	•		○

Figure 10

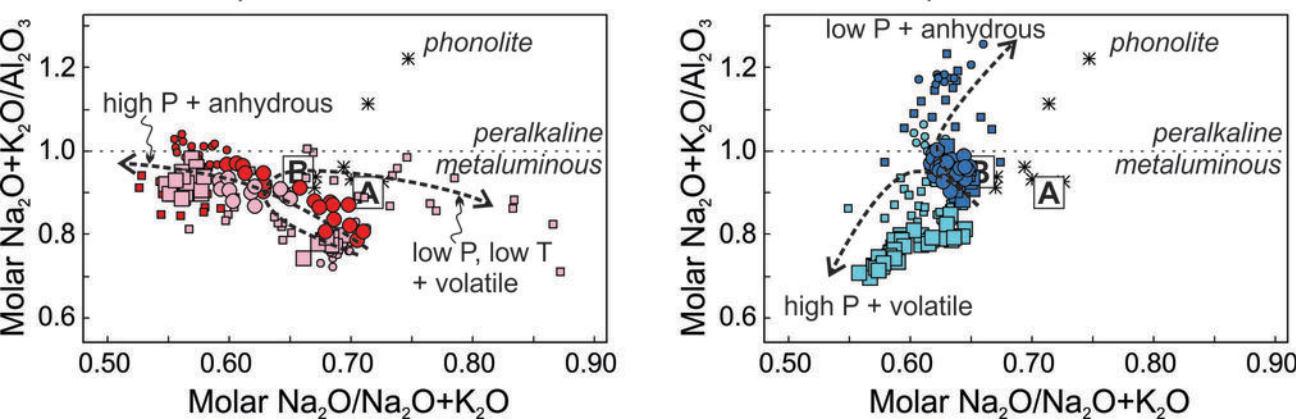
Experimental set A
Experimental set B
phonolite
peralkaline
metaluminous
high P + anhydrous
low P, low T
+ volatile
low P + anhydrous
high P + volatile
A
B
Molar Na2O+K2O/Al2O3
Molar Na2O/Na2O+K2O
1.2
1.0
0.8
0.6
0.50
0.60
0.70
0.80
0.90

Figure 11

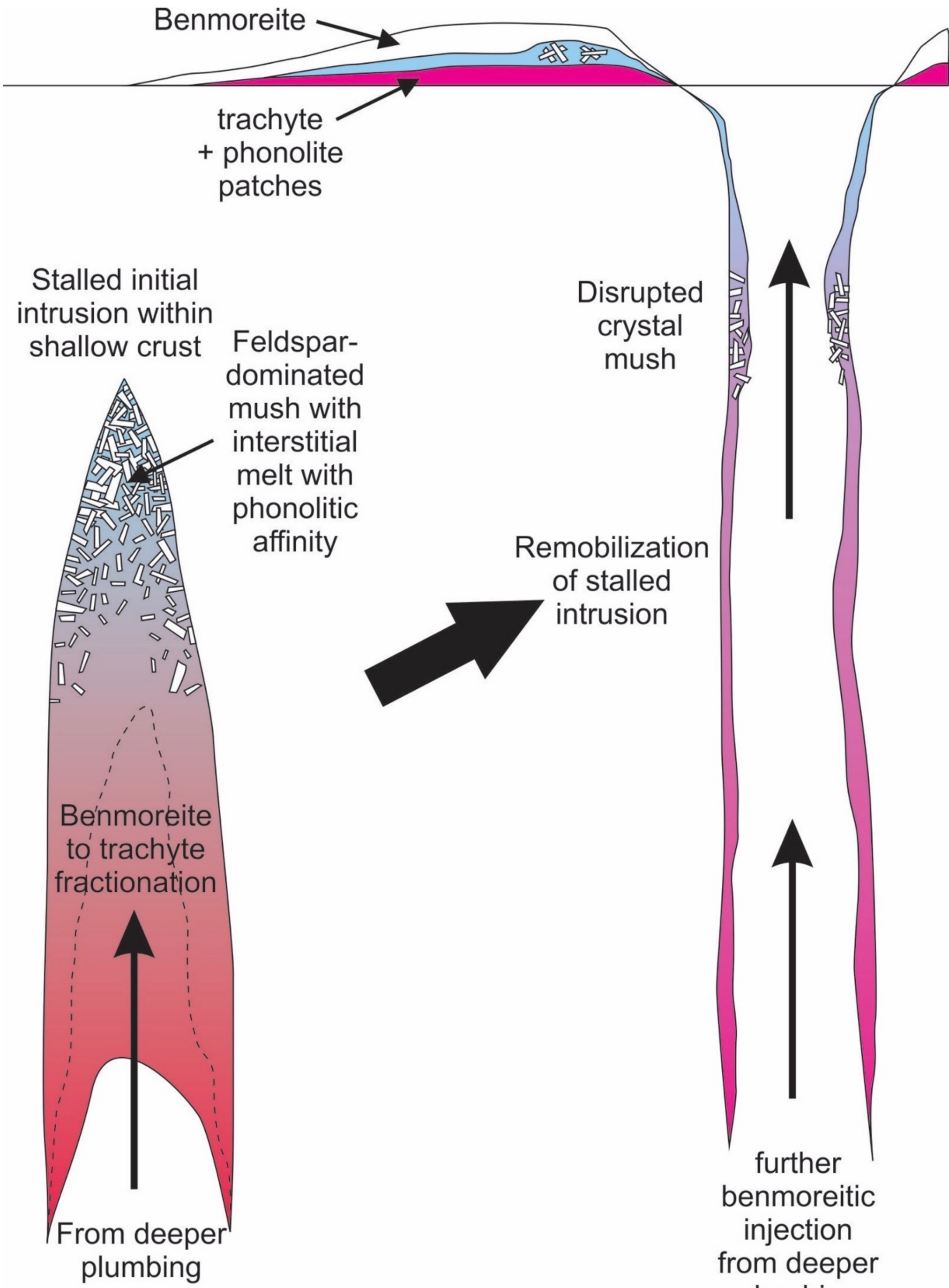
Benmoreite
trachyte
+ phonolite
patches
Stalled initial
intrusion within
shallow crust
Feldspar-
dominated
mush with
interstitial
melt with
phonolitic
affinity
Benmoreite
to trachyte
fractionation
From deeper
plumbing
Disrupted
crystal
mush
Remobilization
of stalled
intrusion
further
benmoreitic
injection
from deeper
plumbing